

DENSITY FUNCTIONAL CALCULATIONS
OF RUBIDIUM UNDER
PRESSURE

by

Anthony Jon Zukaitis

Master of Science
University of Nevada, Las Vegas
1998

Bachelor of Science
University of Wyoming, Laramie
1996

A dissertation submitted in partial
fulfillment of the requirements for the

Doctor of Philosophy Degree
Department of Physics
College of Sciences

Graduate College
University of Nevada, Las Vegas
May 2001

ABSTRACT

Density Functional Calculations of Rubidium under Pressure

by

Anthony J. Zukaitis

Dr. Tao Pang, Examination Committee Chair
Associate Professor of Physics
University of Nevada, Las Vegas

With developments in X-ray diffractometry, experimentalists have been able to resolve the complex structures that had eluded them in the past. One area of this interest is in the regime of alkali metals under pressure. For years, the alkali metals have been viewed as simple systems whose properties can be understood with fairly simple ideas. Under pressure, things get interesting and one observes complex crystal structures in all of the alkali metals under high enough pressure. What is more interesting is that there appears to be many similarities in the phase diagrams of the alkali metals. This hints that this complexity is related to the similarities in the electronic structure of the different alkali metals. Fundamentally, one would like to know more about the electronic structure and its relation to the complex structures observed. This involves solving the Schroedinger equation for the particular system. Unfortunately, this equation is very difficult to solve exactly

for more than two particles and the systems of interest are macroscopic containing on the order of 10^{20} electrons and nuclei.

Since the development of quantum mechanics in 1918, much research has been done on simplifying the many-body Schroedinger equation. In many cases, the simplification of the Schroedinger equation involves making approximations that may or may not be applicable to every system. For the systems of high and nearly uniform density, one of the best approximations is Density-Functional theory. This theory has been used successfully in many calculations of the properties of various systems. Unfortunately, it has also been known to fail as well.

It is my goal in this dissertation to use the density functional method to study solid rubidium at different and extremely high pressures on the order of 10^5 atmospheres. In Chapter 1, the complicated structures of the alkali metals K, Rb, and Cs at high pressure will be discussed. The density functional method and some of the related theories preceding it will be summarized in Chapter 2. Next, in Chapter 3, the pseudopotential approximation, which will be used in conjunction with the density functional method, is described. In Chapter 4, some of the details and theory about implementing both density functional theory and the pseudopotential approximation are highlighted. Finally, in Chapters 5 and 6, the details of the calculations will be discussed. The final conclusions and discussion will be given in Chapter 7.

TABLE OF CONTENTS

ACKNOWLEDGEMENTS	vii
LIST OF FIGURES	viii
LIST OF TABLES	ix
CHAPTER 1: ALKALI METALS UNDER HIGH PRESSURE	1
1.1 Rubidium	1
1.2 Cesium	6
1.3 Potassium	7
1.4 $s \rightarrow d$ transfer	8
CHAPTER 2: DENSITY FUNCTIONAL THEORY	11
2.1 The Born-Oppenheimer Approximation	13
2.2 The Hartree-Fock Approximation	15
2.3 The Thomas-Fermi Model	18
2.4 The Kohn-Sham Hamiltonian	19
2.5 The Kohn-Sham Eigenstates	20
2.6 The Local-Density Approximation	21
2.7 The Car-Parrinello Method	23
2.8 A Quick Example	25
CHAPTER 3: PSEUDOPOTENTIALS	29
3.1 Ghost State Analysis	34
3.2 Pseudo-wavefunction Construction	35
3.3 Nonlinear Core-Valence Corrections	36
CHAPTER 4: COMPUTATIONAL DETAILS	38
4.1 Basis Functions	38
4.2 Basis Representation	39
4.3 Electronic Temperature	42
4.4 Finite \mathbf{k} -Space	43

CHAPTER 5: RUBIDIUM PART I	45
5.1 Pseudopotential Construction	45
5.2 The Pseudopotential Program	48
5.3 Pseudopotential Construction in Practice	49
5.4 Transferability and Occupancies	49
5.5 Further Testing	52
5.6 The PBE Approximation	59
5.7 Discussion	61
CHAPTER 6: RUBIDIUM PART II	62
6.1 Complex Structures	69
6.2 Rubidium IV	72
CHAPTER 7: CONCLUSIONS	79
BIBLIOGRAPHY	80
VITA	84

ACKNOWLEDGEMENTS

First, I would like to thank my advisor Dr. Tao Pang for all the aid and support he has given me throughout the years. To Mr. John Kilburg, thank you for all of help you have given me with the computational aspects my research. To the Bigelow Committee and the High Pressure Science Center, thank you for all of the financial support. I also thank all of my committee members Dr. Changfeng Chen, Dr. Stephen Lepp, and Dr. Kathleen Robins. This dissertation highlights the end of my Graduate Degree. Over the years, I have made many friends with the faculty, staff, and graduate students in the Department of Physics at UNLV; to all of them I owe my gratitude. I also acknowledge the Tuesday Night Beer Crew for helping me maintain my sanity. Finally, I would like to thank my family and especially Shay and Brandon for being supportive and understanding of everything I have done.

LIST OF FIGURES

1.1	Rb IV phase along (001) direction with fully occupied Wyckoff $4b$ sites	3
1.2	Rb IV along the (110) direction with the Wyckoff $8g$ sites highlighted	4
1.3	Rb V,Cs IV structures along the (001) direction	5
1.4	Rb V,Cs IV structure along the (100) direction	5
1.5	Rb VI, Cs V along the (001) direction	6
2.1	Car–Parrinello iterative diagonalization example	28
5.1	Nonlocal pseudopotential components for rubidium	50
5.2	Nonlocal pseudo-wavefunction components for rubidium	50
5.3	Logarithmic derivatives of a pseudopotential for rubidium with a ghost state.	51
5.4	Logarithmic derivatives of a pseudopotential for rubidium with the ghost state removed.	52
5.5	A figure showing the model core to correct for the exchange correlation energy in Rubidium.	56
5.6	Energy-volume for the fcc and bcc structures.	58
5.7	Energy versus volume for the bcc and fcc structures using fcc as the reference.	58
5.8	Enthalpy versus pressure for the bcc structure in comparison to that of the fcc curve.	60
6.1	Energy versus volume comparison for the hard and soft pseudopotentials	65
6.2	Energy versus volume calculation for the hard pseudopotential for the fcc and bcc structures	66
6.3	Enthalpy versus pressure calculations for the hard pseudopotential for the fcc and bcc structures	66
6.4	Band structure for bcc rubidium near zero pressure	67
6.5	Band structure for bcc rubidium near 13 GPa	68
6.6	Density of states for fcc rubidium at two pressures	68
6.7	Energy-volume calculations for the known structures of rubidium	70
6.8	Pressure versus volume calculations for the five known phases of rubidium	71
6.9	Enthalpy-pressure calculations for the known structures of rubidium	71
6.10	Rb IV energy versus c/a for the fully occupied $4b$ sites	73
6.11	A second view of the enthalpy curves with another Rb IV structure	74

LIST OF TABLES

1.1	Experimental transition pressures for rubidium	2
1.2	Transition pressures for the known phases of cesium	7
1.3	Transition pressures for the known phases of potassium	8
5.1	Energy convergence for the soft rubidium pseudopotential for energy cutoff .	53
5.2	Total energy convergence for the soft rubidium pseudopotential for k -points	53
5.3	Fitted values to Murnaghan equation of state for the bcc rubidium structure with out the non linear core valence correction.	54
5.4	Fitted values to Murnaghan equation of state for the bcc rubidium structure with the nonlinear core valence correction.	56
5.5	Transferability comparisons for the bcc pseudopotential	57
5.6	Equation of state data for the bcc calculation using the PBE functional . . .	60
5.7	Transferability tests for the PBE pseudopotential	61
6.1	Murnaghan parameters for both the soft and hard potentials.	64
6.2	A list of the possible occupancies of the Wyckoff $4b$ sites in the Rb IV structure.	75
6.3	Energies for the different configurations listed in Table 6.2	76
6.4	Selected configurations for the Rb IV structure which is doubled in size along the z axis	77
6.5	Here are the listed energies for the various possible configurations for atoms in the $4b$ sites listed in Table 6.4.	77

CHAPTER 1

ALKALI METALS UNDER HIGH PRESSURE

Rubidium is one of the alkali metals in the first column of the periodic table. Alkali metals are considered to be simple since they have only one electron in the valence shell. In the past few years, complex structures have been observed and identified in these simple metals under high pressure [1-7] and it is quite unusual. Many of these complex crystal structures have been observed in the heavy alkali metals potassium, rubidium, and cesium. Although complex structures have also been identified in lithium [1], they do not appear to be related to the structures seen in the heavier alkalis. However, in K, Rb, and Cs, there do appear to be similarities among their phase diagrams. I will highlight some of these similarities here and make some general comparisons among these three alkalis. The current understanding of the physics behind these structures will be discussed toward the end of this chapter.

1.1 Rubidium

At atmospheric pressure and room temperature, it is understood that the alkali metals have the body-centered cubic (bcc) structure. Under increased pressure, the alkali metals K, Rb, and Cs, have a phase transition from the bcc structure to the

Phase Transition		Transition Pressure (GPa)
bcc	→ fcc	7
fcc	→ ? (III)	12
? (III)	→ $I4/mcm$ (IV)	17
$I4/mcm$ (IV)	→ $I4_1/amd$ (V)	20
$I4_1/amd$ (V)	→ $Cmca$ (IV)	46

Table 1.1: A list of the known phases and the corresponding pressure points for the structural transitions of rubidium at room temperature. Each phase is identified in this table by the space group associated with the structure.

face centered cubic (fcc) structure. These structures are favored because of the spherically symmetric s orbitals of the outermost electrons. Since they are spherically symmetric atoms, they would favor the structures that have the highest packing fractions like the fcc or hexagonal closed packed (hcp) structures. It turns out that under a further increase in pressure, the systems favor low symmetry structures which have small packing fractions.

At pressures above that of the fcc phase, extremely complex structures are observed in all of the alkali metals. In Table 1.1, a list of the known phase transitions of rubidium is shown. At 12 GPa, there is a phase transition to the currently unidentified structure which is referred to as Rb III [2]. It is believed that this structure may be similar to Rb III of potassium [8].

At 17 GPa, another phase transition is observed to the complex phase of Rb IV [4]. One solution to the structure is shown in Fig. 1.1. The symmetry of the structure has been experimentally identified to belong to the space group $I4/mcm$. Although the space group of the structure has been determined, the basis is not

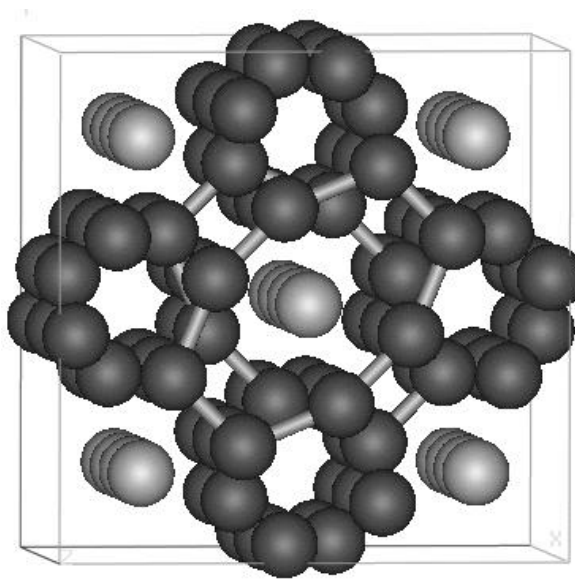


Figure 1.1: The structure of Rb IV. Here the Wyckoff 4b sites are fully occupied as indicated by the lighter spheres. The dark spheres occupy the Wyckoff 16k sites and form columns along the z axis. The bonds connecting the spheres highlight the elliptical set of atoms confining each 4b site.

quite resolved. The structure is estimated to have approximately 20 atoms per unit cell. Along the z axis are columns formed by alternating squares of rubidium atoms occupying the Wyckoff 16k sites. In the channels are other rubidium atoms whose positions are not quite clear.

In Fig. 1.2 a cut of the Rb IV structure along the (110) direction is shown with next possible solution. Experimentally, the best fit to the data is half occupancy of the Wyckoff 8g sites. The next best fit, is a full occupancy of the Wyckoff 4b sites which are sites centered in between the pairs of 8g sites shown in Fig. 1.2. The fact that the experimental results are not conclusive leads to the possibility for the structure of Rb IV to be disordered, which has not been observed in any of the other

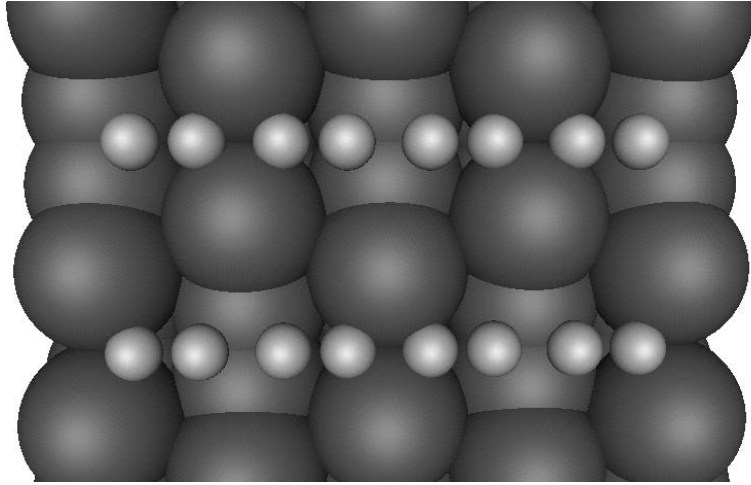


Figure 1.2: Another view of the Rb IV structure along the (110) direction. The lighter spheres in this figure are the Wyckoff $8g$ sites that are proposed to be half occupied [4]. The Wyckoff $4b$ sites are not shown but would be directly centered on each pair of $8g$ sites. The sizes of the spheres have been altered to give the reader a better view of the geometry of the sites.

alkali metals under pressure to date.

At 20 GPa a phase transition from Rb IV to a less complex phase with an orthorhombic structure with 4 atoms per unit cell [2] is experimentally observed and. Two views of the structure are shown in Figures 1.3 and 1.4. The structure of this phase belongs to the space group $I4_1/amd$. This structure has a large c/a of approximately 3.7 which is the ratio of the length of the z axis of the unit cell to the length of the x axis. The structure can be viewed as a set of layers of squares, with each layer slightly offset in the xy plane. There are four offset layers at $z = 0.00c, 0.25c, 0.50c, 0.75c$. This phase persists up to approximately 46 GPa where a transition to Rb VI, another complex structure, occurs.

The structure of the Rb VI phase belongs to the space group $oC16$ and has full

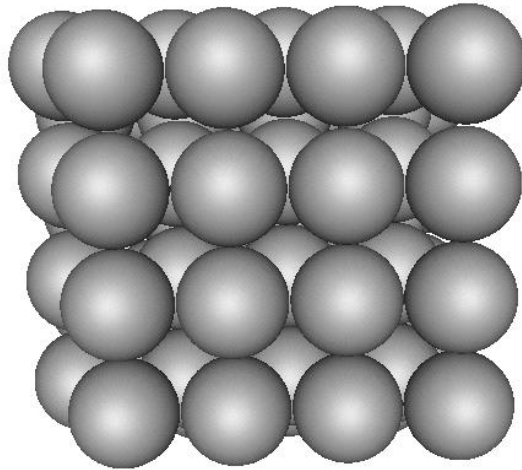


Figure 1.3: A picture of Rb V whose structure is similar to Cs IV. The view point is along the (001) direction and the unit cell is repeated four fold along each of the x and y axis.

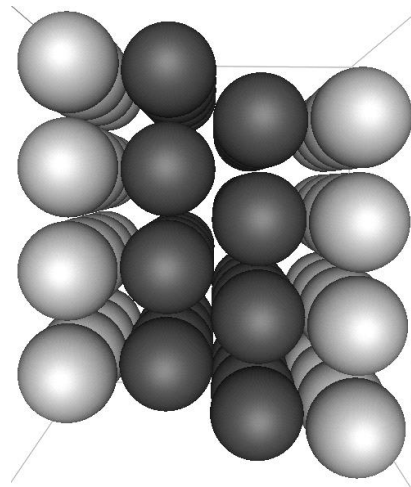


Figure 1.4: This is Rb V, Cs IV shown along the (100) direction. The darker planes are going into the page whereas the lighter planes are coming out.

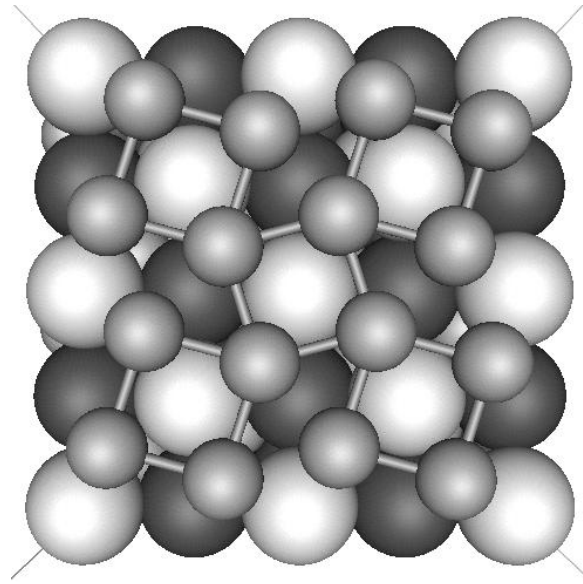


Figure 1.5: A picture of Rb VI, which is similar to Cs V. The viewpoint of this figure is along the (001) direction. The small, light spheres signify the atoms in the $8f$ sites and the large spheres are the atoms in the Wyckoff $8d$ sites. The lighter $8d$ spheres are coming out of the plane whereas the darker ones are going into the plane.

occupancy of the Wyckoff $8f$ and $8d$ sites corresponding to 16 atoms per unit cell.

The structure of the Rb VI phase is shown in Fig. 1.5. The structure viewed along the (001) direction is layered. The top layer formed by the $8f$ atoms forms a layer of buckled squares. Underneath this layer is another layer of the $8d$ atoms that buckles slightly along the z direction.

1.2 Cesium

The phase transitions observed in cesium closely follow the transitions seen in rubidium. Cesium is just one row below rubidium on the periodic table which gives

Phase Transition		Transition Pressure (GPa)
bcc	→ fcc	2.3
fcc	→ Collapsed fcc	4.2
Collapsed fcc	→ $I4_1/amd$ (IV)	4.3
$I4_1/amd$ (IV)	→ $oC16$ (V)	10
$oC16$ (V)	→ dhcp (VI)	72

Table 1.2: A list of the known phases and the corresponding pressure points for the structural phase transitions for cesium at room temperature. The phases are listed by their index and the space group of the structure.

it a similar valence electronic configuration but a larger mass. There are six known structural phase transitions which are listed in Table 1.2.

A bcc to fcc transition which is also observed in Cs at a lower pressure point than the same transition observed in potassium and rubidium. The two phases above 4.3 GPa, Cs IV and V correspond to the same structures of Rb V and VI respectively. The pressure points for the corresponding transitions in rubidium are in general much higher. For example, the Cs IV to Cs V transition pressure occurs at 10 GPa whereas in rubidium it is around 46 GPa. With such a similarity between Cs and Rb one might expect that Rb would have the double hexagonal closed packed (dhcp) structure in some higher pressure regime. Structures similar to the Rb III and Rb IV structures are not observed in cesium.

1.3 Potassium

There have only been two phase transitions observed in potassium. A list of the phase transitions in potassium is given in Table 1.3. The pressure point for the bcc

Phase Transition	Transition Pressure (GPa)
bcc (I) \rightarrow fcc (II)	11.6
fcc(II) \rightarrow $I4mmm$? (III)	23

Table 1.3: A list of the known phases and the corresponding pressures for the structural transitions for potassium at room temperature. The question mark for K III indicates that the structure for this phase is unknown.

to fcc transition in potassium is 11.6 GPa. The pressure point for this transition is about 4 GPa higher than the pressure point for the same transition in Rb. Interestingly enough, the space group for K III has been identified, yet the structure has not [2]. It is also rumored that the Rb III structure is similar to that of K III [8]. This would not be unreasonable since the published X-ray data for the structures appears similar in these phases.

Theoretically, it is understood that all of these complex transitions are driven by changes in the electronic structure. One of the most important calculations that has been done to date on the alkali metals is the work by McMahan [13]. This work has provided some insight into the physics behind the complex phases seen in the alkali metals at high pressure.

1.4 $s \rightarrow d$ transfer

In 1984, McMahan published some calculations on the compression of Cs, Rb and K [13]. Using the LMTO method [12], he was able to show how the orbitals, or bands, change under pressure. He was able to show that under increasing pressure,

the valence s band rises above the valence d band in K, Rb, and Cs. As this occurs the occupation of the d band increases thus giving the metal a stronger d character under pressure.

McMahan's work for cesium indicates that as the pressure is increased the $5d$ level becomes lower in energy than the $6s$ at about 15 GPa with the $6s$ band crossing the Fermi level. At this pressure, there is no occupation of the $6s$ band but a full occupation of the $5d$ band. It is this transfer of electrons from the $6s$ band to the $5d$ band that is believed to be the reason for the complex structures of Cs IV and Cs V. Under further compression, McMahan showed that the core $5p$ bands also becomes higher or comparable in energy to the $5d$ bands. Since the $5p$ bands are fully occupied, the Pauli repulsion is the driving mechanism for the dhcp phase at 72 GPa.

McMahan also gave estimates for the pressure where the $s \rightarrow d$ transfer would become complete. For Cs, Rb, and K the pressure points are at 15, 53, and 60 GPa, respectively. In Cs and Rb, this end of the transition corresponds to the Rb V to Rb VI transition and the same structural transition in Cs IV to Cs V.

At the time of his publication, nothing was known about the structures or lattices of the complex phases. All of his comparisons were done with the simple structures fcc, bcc, and dhcp. Throughout all of the experimental work on K, Rb, and Cs the $s \rightarrow d$ transition is always highlighted. In June of 2000, K. Takemura *et al.* [14] published calculations on the stability of the high pressure phases of cesium and

confirmed the experimental observations.

There are other calculations and studies on the alkali metals with a focus on the bcc to fcc transition [9, 10, 11]. Most of these results have demonstrated that first principles calculations can provide reasonable accuracy for the bcc to fcc transition pressure and equation of state parameters. Calculations for the complex, high pressure phases for rubidium and potassium have not been accomplished until now. This dissertation provides one of the very first attempts to calculate the energies to analyze the stabilities of the high pressure phases of Rb from first principles calculations. From these results we will attempt to obtain a theoretical explanation for the complex crystal structures observed in recent X-ray experiments.

CHAPTER 2

DENSITY FUNCTIONAL THEORY

Density functional theory is a method to reduce a many-body Hamiltonian a set of equations which are effectively one electron Schroedinger equations. I will focus on some of the related history leading to density functional theory(DFT) because many techniques used in DFT had been introduced in some other previous methods to study a many-body Hamiltonian.

I will start the discussion with the time-independent Schroedinger equation for a system of electrons and nuclei:

$$\hat{H}(\mathbf{r}, \mathbf{R}) \Psi_n(\mathbf{r}, \mathbf{R}) = E_n \Psi_n(\mathbf{r}, \mathbf{R}), \quad (2.1)$$

where \hat{H} is the Hamiltonian operator, E_n is the energy eigenvalue, and $\Psi_n(\mathbf{r}, \mathbf{R})$ is the corresponding eigenfunction of the Hamiltonian. Here \mathbf{r} is defined as the complete set of electron coordinates and spins.

$$\mathbf{r} = \{\mathbf{r}_1\sigma_1, \mathbf{r}_2\sigma_2, \dots, \mathbf{r}_N\sigma_N\} \quad (2.2)$$

Similarly, \mathbf{R} the complete set of nuclei coordinates.

In general, the Hamiltonian for a many-body system is complicated, to which a solution is usually unavailable. The Hamiltonian operator for a system of electrons and nuclei, expressed in the Hartree units ($\hbar = 1$, $m_e = 1/2$, $e^2 = 2$), is

$$\hat{H} = - \sum_i \nabla_i^2 - \sum_J \frac{1}{2M_J} \nabla_J^2 + V_{ee} + V_{eN} + V_{NN}, \quad (2.3)$$

where the summations are carried over all of the electrons, and their spin through index i and J for the nuclei. I will use the following convention throughout this dissertation: summations over lower-case indices are for electrons and summations over upper-case indices are for the nuclei. In Eq. (2.3), M_J is the mass of the nuclei, V_{ee} represents the potential energy operator for the electron electron interactions, V_{eN} is the potential energy operator for the electrons-nucleus interaction and V_{NN} is the potential energy between the nuclei. The interaction terms in Eq. (2.3) are two-body Coulomb interactions:

$$V_{ee} = \sum_{i \neq j} \frac{1}{|\mathbf{r}_i - \mathbf{r}_j|}, \quad (2.4)$$

$$V_{eN} = \sum_{i,J} \frac{z_J}{|\mathbf{r}_i - \mathbf{R}_J|}, \quad (2.5)$$

and

$$V_{NN} = \sum_{I \neq J} \frac{z_I z_J}{|\mathbf{R}_I - \mathbf{R}_J|} \quad (2.6)$$

where z_I is the nuclear charge of the I_{th} nucleus.

So far we have made no approximations to the Schroedinger equation. It has been stated in order to present the root of the many-body problem. This equation is almost impossible to solve analytically for more than two particles. For more particles, one must resort to an elaborate scheme, typically numerical, to diagonalize the Hamiltonian and it usually becomes an enormous task even by today's computational standards.

2.1 The Born-Oppenheimer Approximation

In many of the approximations to the many-body Schroedinger, one can approximate the many-body wave function $\Psi_n(\mathbf{r}, \mathbf{R})$ as fully separable. This is the so-called Born-Oppenheimer approximation which is also referred to as the adiabatic approximation. This assumes the wave function, $\Psi_n(\mathbf{r}, \mathbf{R})$, can be written as

$$\Psi_n(\mathbf{r}, \mathbf{R}) = \Phi(\mathbf{r}, \mathbf{R})\Gamma(\mathbf{R}) \quad (2.7)$$

where \mathbf{r} and \mathbf{R} are the coordinates and spins of the electrons and nuclei respectively. Using this form of the wave function, one can split up the Hamiltonian into two parts and as a consequence, we need to solve the following two equations:

$$\hat{H}_e\Phi(\mathbf{r}, \mathbf{R}) = \epsilon\Phi(\mathbf{r}, \mathbf{R}) \quad (2.8)$$

and

$$\hat{H}_{nuc}\Gamma(\mathbf{R}) = \epsilon_{nuc}\Gamma(\mathbf{R}). \quad (2.9)$$

These Hamiltonians are defined as

$$\hat{H}_e = - \sum_i \nabla_i^2 + V_{ee} + V_{Ne} \quad (2.10)$$

and

$$\hat{H}_{nuc} = - \sum_J \frac{1}{2M_J} \nabla_J^2 + V_{NN} \quad (2.11)$$

where the corresponding eigenvalues of the Hamiltonians are ϵ and ϵ_{nuc} , respectively.

Normally, one would consider $\Phi(\mathbf{r}, \mathbf{R})$ a function of \mathbf{r} alone for fixed \mathbf{R} , but we will leave this dependence in for the moment. In the above approximation, it was assumed that the following term could be neglected:

$$\sum_J \frac{1}{2M_J} \nabla_J^2 \Phi(\mathbf{r}, \mathbf{R}). \quad (2.12)$$

This term can be approximated to be of the order $\sqrt{\frac{m_e}{M_J}}$ [15]. The result is that the electronic system is assumed to always be in the ground-state, independent of the motion of the nuclei yet dependent of their position. In other words, the system is adiabatic and no heat is allowed to be exchanged between the electrons and nuclei. If the approximation is appropriate, the resulting problem is to solve Eq. (2.8) which represents a system of electrons in the field of a set of fixed nuclei.

2.2 The Hartree-Fock Approximation

For future reference, the functional dependence on \mathbf{R} will not be given explicitly, with the understanding of its role as stated above. Further more, the notation \mathbf{r} now pertains to a single coordinate. In 1928, Hartree proposed a simple approximation with the many electron wave function $\Phi(\mathbf{r})$ written as a product of single electron wave functions [16, 17],

$$\Phi(\mathbf{r}_1, \mathbf{r}_2, \mathbf{r}_3, \dots) = \prod_i \phi_i(\mathbf{r}_i). \quad (2.13)$$

Using the Variational approach to the ground-state energy of the system with respect to $\phi_i(\mathbf{r}_i)$, one finds that the ground state energy is minimized by a set of equations similar to the Schroedinger equation for a single-electron moving in an external field

$$\left\{ -\nabla^2 + V_{ext}(\mathbf{r}) + V_H(\mathbf{r}) \right\} \phi_i(\mathbf{r}) = \epsilon_i \phi_i(\mathbf{r}), \quad (2.14)$$

where $V_H(\mathbf{r})$ is the Hartree potential

$$V_H(\mathbf{r}) = \int \frac{\rho(\mathbf{r}') d\mathbf{r}'}{|\mathbf{r} - \mathbf{r}'|}, \quad (2.15)$$

and $V_{ext}(\mathbf{r})$ is the potential field arising from the nuclei or any other static, external potential. $\rho(\mathbf{r})$ is the electron density function

$$\rho(\mathbf{r}) = \sum_j |\phi_j(\mathbf{r})|^2, \quad (2.16)$$

which is just the sum of the probability densities of the individual one electron states. In some approximations, the self interaction of a state with itself is subtracted in the form

$$\left\{ -\nabla^2 + V_{ext}(\mathbf{r}) + V_H(\mathbf{r}) - \int \frac{|\phi_i(\mathbf{r}')|^2 d\mathbf{r}'}{|\mathbf{r} - \mathbf{r}'|} \right\} \phi_i(\mathbf{r}) = \epsilon_i \phi_i(\mathbf{r}). \quad (2.17)$$

where

$$\int \frac{|\phi_i(\mathbf{r}')|^2 d\mathbf{r}'}{|\mathbf{r} - \mathbf{r}'|}, \quad (2.18)$$

is the self interaction term. The above approximation is the Hartree approximation. This approximation does not include any Fermi statistics and a couple years later they were incorporated into the Hartree approximation to give the Hartree-Fock approximation [16, 17]. This approximation follows the same path as the Hartree approximation except that one applies the variational principle to a wave function of the form of a Slater determinant:

$$\Phi(\mathbf{r}_1, \mathbf{r}_2, \mathbf{r}_3, \dots, \mathbf{r}_N) = \begin{vmatrix} \phi_1(\mathbf{r}_1) & \phi_2(\mathbf{r}_1) & \dots & \phi_N(\mathbf{r}_1) \\ \phi_1(\mathbf{r}_2) & \phi_2(\mathbf{r}_2) & \dots & \phi_N(\mathbf{r}_2) \\ \vdots & \vdots & & \vdots \\ \phi_1(\mathbf{r}_N) & \phi_2(\mathbf{r}_N) & \dots & \phi_N(\mathbf{r}_N) \end{vmatrix}. \quad (2.19)$$

The Slater determinant is a compact way to represent the full antisymmetric form of the electronic wave function. In this equation, N is the number of electrons. After the variational principle is applied, one finds that there is an additional term to the Hartree equation stated earlier in Eq. (2.14). This additional term is the exchange energy which is defined as

$$V_{ex}(\mathbf{r}) = -2 \sum_{j \neq i} \delta(\sigma_i, \sigma_j) \phi_j(\mathbf{r}) \int \frac{\phi_j^*(\mathbf{r}') \phi_i(\mathbf{r}')}{|\mathbf{r} - \mathbf{r}'|} d\mathbf{r}' \quad (2.20)$$

where σ_i is the spin component of spin of the i_{th} electron. This term is called the exchange interaction between electrons of the same spin. This term produces a spatial separation between electrons of the same spin and thus reduces the Coulomb energy of the system. As a result the Hartree Fock approximation gives

$$\{-\nabla^2 + V_{ext}(\mathbf{r}) + V_H(\mathbf{r})\} \phi_i(\mathbf{r}) + V_{ex}(\mathbf{r}) \phi_i(\mathbf{r}) = \epsilon_i \phi_i(\mathbf{r}). \quad (2.21)$$

It is known that the energy of the system can be reduced below its minimum Hartree-Fock energy if electrons of opposite spin are also spatially separated. This is referred to as the Correlation Energy. The Correlation Energy is defined as the difference between the exact many body energy and Hartree Fock energy of an electronic system. This means that to find the correlation energy of the system, one must already have the exact solution which can only be obtained by directly diagonalizing the full Hamiltonian of Eq. (2.10).

2.3 The Thomas–Fermi Model

Around 1927, Thomas and Fermi came up with the idea to simplify the many–body Hamiltonian even further [18, 19]. The main idea is to focus on the local electron density and not the wavefunctions themselves. The Thomas–Fermi approximation for the energy of an electron density in an external potential is

$$E_{TF}[\rho(\mathbf{r})] = C_F \int \rho^{5/3}(\mathbf{r}) d\mathbf{r} - \int \rho(\mathbf{r}) V_{ext}(\mathbf{r}) d\mathbf{r} + \frac{1}{2} \int \int \frac{\rho(\mathbf{r})\rho(\mathbf{r}')}{|\mathbf{r} - \mathbf{r}'|} d\mathbf{r} d\mathbf{r}' \quad (2.22)$$

and

$$C_F = \frac{3}{10}(3\pi^2)^{2/3} = 2.871. \quad (2.23)$$

This energy is minimized under the constraint

$$\int \rho(\mathbf{r}) d\mathbf{r} = N_e, \quad (2.24)$$

where N_e is the total number of electrons in the system. In this model, all of the Coulomb interactions are treated classically and the kinetic energy of the electrons, $C_F \int \rho^{5/3}(\mathbf{r}) d\mathbf{r}$, is derived using Fermi statistics. Although model is rather simplified, it does lead to an important idea: minimizing the total energy with respect to the electron density point-to-point in the entire space.

2.4 The Kohn–Sham Hamiltonian

In 1964, Hohenberg and Kohn proved that there exists a one-to-one mapping between exact ground-state electron density distribution and the exact ground-state energy of the system [20]. Their proof showed that two different external, local potentials cannot be minimized by the same electron density distribution. This means that one can minimize an expectation value of the exact many body Hamiltonian to its ground state by varying the electron density distribution alone. The Hohenberg-Kohn theorem allows one to define a density functional:

$$E[\rho(\mathbf{r})] = T^s[\rho(\mathbf{r})] + E^H[\rho(\mathbf{r})] + E^{e-nuc}[\rho(\mathbf{r})] + E^{xc}[\rho(\mathbf{r})] + E^{nuc-nuc} \quad (2.25)$$

where E is the total energy of the system, $T^s[\rho(\mathbf{r})]$ is the kinetic energy of the non-interacting electrons, E^H is the Hartree energy, E^{xc} is the exchange-correlation energy, and $E^{nuc-nuc}$ is the interaction energy among the nuclei, which is already assumed to be independent of the electron density under the Born-Oppenheimer approximation. Here the exchange and correlation energies of the electrons are combined into one term $E^{xc}[\rho(\mathbf{r})]$. This functional can be evaluated exactly, provided the correct form of $E^{xc}[\rho(\mathbf{r})]$ is known.

2.5 The Kohn–Sham Eigenstates

In this section we will obtain the Kohn-Sham eigenstates [21]. First the one-body electron density is defined as

$$\rho(\mathbf{r}) = \sum_i |\phi_i(\mathbf{r})|^2. \quad (2.26)$$

Again the variational approach is taken with respect to the $\phi_i(\mathbf{r})$ and one arrives at an equation similar to the Hartree-Fock equation. This gives

$$\hat{H}_{ks}|\phi_i\rangle = \epsilon_i|\phi_i\rangle, \quad (2.27)$$

where the Kohn-Sham [21] Hamiltonian \hat{H}_{ks} is defined as

$$\hat{H}_{ks} = -\nabla^2 + V_{ext}(\mathbf{r}) + V_H(\mathbf{r}) + V_{xc}(\mathbf{r}). \quad (2.28)$$

This single-particle Hamiltonian is very similar to the Hartree-Fock Hamiltonian except projected to one state. Now we have combined the exchange and correlation terms in to $V_{xc}(\mathbf{r})$. This still leaves one at the point where one does not know the Correlation Energy. The exchange energy can be evaluated exactly, but it is computationally expensive to calculate [22]. Therefore in many approximations, these contributions are treated together to simplify the calculation. For example, one may want to approximate the exchange interaction to make it a local operator.

This can be done as long as one knows the gross error that is caused by such an approximation.

As far as the correlation energy goes, there is no easy way out. To get the correlation energy, we need to know the exact total energy of the system. However, we may make a few more drastic, yet viable approximations. One route is to calculate the exchange-correlation energy exactly in one system and then apply the result to another system.

2.6 The Local-Density Approximation

Many approximations exist for the exchange-correlation energy of a system of interacting electrons. The most popular and simplest approximation is the local-density approximation. The approximation begins by assuming that the exchange-correlation energy for the electrons is independent of the environment or potential. Or in other words, the exchange-correlation energy of any electron density, is the same as that for a homogenous electron gas. Let $\chi(\mathbf{r})$ be the exchange correlation energy for a single electron at a point \mathbf{r} in the gas at the same local density. Then the exchange-correlation energy of the total system is given by

$$E_{xc}[\rho(\mathbf{r})] = \int \chi(\mathbf{r})\rho(\mathbf{r})d\mathbf{r}, \quad (2.29)$$

that can be used to obtain the exchange-correlation potential

$$V_{xc}(\mathbf{r}) = \frac{\delta E_{xc}[\rho(\mathbf{r})]}{\delta \rho(\mathbf{r})}. \quad (2.30)$$

Then as a requirement from the functional variation,

$$\frac{\delta E_{xc}[\rho(\mathbf{r})]}{\delta \rho(\mathbf{r})} = \frac{\delta[\rho(\mathbf{r})]\chi(\mathbf{r})}{\delta \rho(\mathbf{r})}. \quad (2.31)$$

Of the many approximations for $\chi(\mathbf{r})$, we will be using the results of Ceperly and Alder [23], which are fitted to the parameterization of Perdew and Zunger [24]. This is done by computing both the Hartree-Fock energy and the exact energy of an interacting electron gas. Once the difference is obtained the result is parameterized in the following manner. First we define an average radius of an electron in the system, r_s , with

$$n = \frac{1}{\frac{4}{3}\pi r_s^3} \quad (2.32)$$

where n is the average electron density. The parameterization of Perdew and Zunger [24] in terms of the plasma radius is

$$\chi(r_s) = A_i \log r_s + (B_i - \frac{1}{3}A_i) + \frac{2}{3}C_i r_s \log r_s + \frac{1}{3}(2D_i - C_i)r_s \quad (2.33)$$

where A_i, B_i, C_i, D_i are parameters chosen to fit the exchange and correlation energy obtained from quantum Monte Carlo simulations done by Ceperly and Alder [23].

2.7 The Car–Parrinello Method

To find the solutions of the Kohn–Sham Hamiltonian, one must solve them self-consistently. This means choosing an electron density, diagonalizing the Hamiltonian to find the Kohn–Sham eigenstates that are consistent to the electron density chosen. The electron density is then redefined in terms of the Kohn–Sham eigenstates. This process is repeated over and over again until the electron density is stationary or at least converged within some tolerance.

For a large basis set, the diagonalization of the Hamiltonian becomes very demanding, computationally. The Car–Parrinello method [25] is a unique scheme in finding the Kohn–Sham eigenstates without the need to directly diagonalize the Hamiltonian. The Car–Parrinello method defines a Lagrangian for the Kohn–Sham eigenstates and treats the eigenstates as dynamical variables that evolve under a fictitious time variable. The Lagrangian for the Kohn–Sham eigenstates ϕ_i is

$$L = \mu \sum_i \langle \dot{\phi}_i | \dot{\phi}_i \rangle - E[\rho(\mathbf{r})] \quad (2.34)$$

where μ is a fictitious mass and $E[\rho(\mathbf{r})]$ is the energy functional of Eq. (2.25). $\dot{\phi}_i$ is the fictitious time derivative of the state ϕ_i . This Lagrangian does not describe the true dynamics of the eigenstates, rather it describes the fictitious dynamics of a set of trial wavefunctions that are forced to evolve to the ground–state wavefunction. This is also referred to as simulated annealing. One must impose one additional

constraint on the solutions to keep all of the states out of the ground state; that is, they must be orthogonal to each other,

$$\langle \phi_i | \phi_j \rangle = \delta_{i,j}. \quad (2.35)$$

Otherwise, every solution would evolve directly to the ground state. The equations of motion of the eigenstates are derived from the Lagrange equation of motion,

$$\frac{d}{dt} \left(\frac{\delta L}{\delta \dot{\phi}_i^*} \right) = \frac{\delta L}{\delta \phi_i^*}. \quad (2.36)$$

If one evaluates the derivatives, one obtains

$$\mu \ddot{\phi}_i = -\hat{H}_{ks} \phi_i + \sum_j \Lambda_{i,j} \phi_j \quad (2.37)$$

where $\Lambda_{i,j}$ are the Lagrange multipliers corresponding to the orthonormality constraint of Eq. (2.35) and \hat{H}_{ks} is the Kohn–Sham Hamiltonian of Eq. (2.28). Because of the complications of evaluating of each Lagrange multiplier, orthogonality is handled by either the Graham–Schmidt method or the Car–Parrinello method at every fictitious time step. In first case case, the states should always be orthogonalized in order of increasing energy to improve efficiency of the iterative scheme. The second

method subtracts off half the overlap of each state with the other states,

$$|\phi'_i\rangle = |\phi_i\rangle - \frac{1}{2} \sum_{j \neq i} \langle \phi_i | \phi_j \rangle |\phi_j\rangle, \quad (2.38)$$

Here the new state $|\phi'_i\rangle$ at each step is generated from the old state $|\phi_i\rangle$ minus 1/2 the overlap of itself with the other states. After the orthogonalization is carried out, one must also renormalize each state.

2.8 A Quick Example

The Car–Parrinello method seems a bit abstract. In this section, I will use a simple example to show how this iterative process works. One of the most fundamental problems in quantum mechanics is the one–dimensional infinite square well. For this problem, I will use a single electron to avoid complicating the problem with electron–electron interactions. One can start from the time–independent Schroedinger equation

$$-\frac{d^2}{dx^2} \phi_n(x) + V(x)\phi_n(x) = E_n \phi_n(x) \quad (2.39)$$

which we have expressed in Hartree units. For the potential

$$V(x) = \begin{cases} 0, & \text{if } 0 \leq x \leq 1; \\ \infty, & \text{otherwise} \end{cases} \quad (2.40)$$

the eigenstates are

$$\phi_n(x) = \sqrt{2} \sin n\pi x. \quad (2.41)$$

Here the length of the square well is 1 bohr. This potential is exactly solvable, so to make things more interesting, the potential is changed to

$$V(x) = \begin{cases} 40x, & \text{if } 0 \leq x \leq 1; \\ \infty, & \text{otherwise} \end{cases} \quad (2.42)$$

which is a sloped square well sloped to the left. One way to solve this problem is to calculate the matrix of the Hamiltonian on the basis of Eq. (2.41) and diagonalize it directly. For a small basis set this is quite fast but the point here is to demonstrate how the Car–Parrinello method works

We will use only four basis functions which corresponds to an energy cutoff of $16\pi^2$ Ht. Again, for simplicity, we will only look at the ground state. First we expand the ground–state eigenfunction $\psi_0(x)$ in the basis set established by Eq. (2.41).

$$\psi_0(x) = \sum_{i=1}^4 c_i \phi_i(x) \quad (2.43)$$

To integrate the fictitious equation of motion for the eigenstate, the Verlet algorithm [26, 27] is used. After some simplification, the equation of motion for each c_i is

$$c_i(t + \delta t) = 2c_i(t) - c_i(t - \delta t) + \lambda(t)c_i(t) - \delta t^2 \sum_{j=1}^4 H_{j,i}c_j(t), \quad (2.44)$$

where

$$H_{j,i} = \langle \phi_j | \hat{H} | \phi_i \rangle \quad (2.45)$$

and

$$\lambda(t) = \sum_{i,j}^4 c_i(t)c_j(t)H_{i,j}. \quad (2.46)$$

In Figure 2.1, the evolution of the trial wavefunction to the exact ground state is shown. The $\delta t = 0.316$ was used for the fictitious time and the wavefunctions are shown at every time step. As one can see the exact solution for the ground state is obtained at $t = 10$ within any visible error.

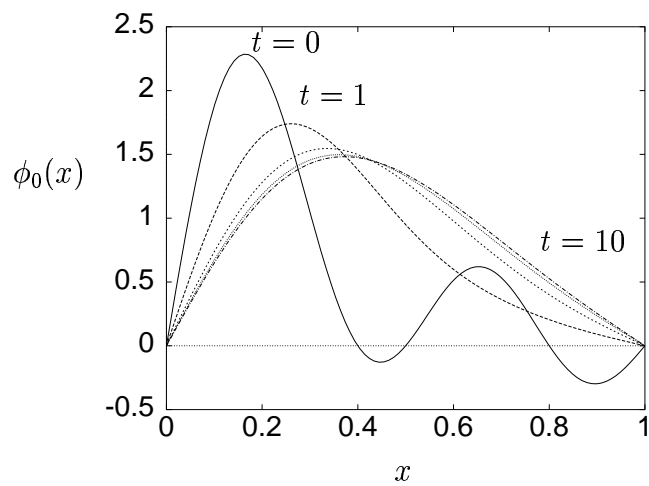


Figure 2.1: A figure showing the convergence of the trial wavefunction at $t = 0$ to the nearly exact wavefunction at $t = 10$.

CHAPTER 3

PSEUDOPOTENTIALS

In general, density functional calculations are computationally demanding for real materials with many electrons and nuclei. The calculations carried out here adopt a plane wave basis. This choice of the basis set creates a problem due to the large number of plane waves required to treat the tightly bound core states. By incorporating pseudopotentials into these calculations, the computational effort can be reduced significantly.

It will be assumed that the core states of the atom play a small role in determining the properties of a solid. As a result, we are assuming that only the occupied valence states are involved in the interactions with other atoms. Although this concept is widely accepted, one must be cautious and be aware that this approximation may fail. To reduce the computational demands of the calculation, the interaction between the core region and valence electrons will be modeled as an interaction between valence electrons and a potential which is termed a pseudopotential.

There are mainly three reasons for incorporating pseudopotentials into DFT calculations. The first reason was mentioned in the previous paragraph. The second problem arises from trying to describe a Coulomb potential with plane waves. In the

density functional calculations, the potential is expressed as matrix elements in k -space. The problem is that a Coulomb potential in k -space goes as $\frac{1}{|\mathbf{k}|^2}$, \mathbf{k} being the radial wavevector. The third reason is that the valence electronic states are highly oscillatory. These oscillations are required to maintain the orthogonality between the valence and core electron states. These oscillations require a large number of plane waves to obtain an adequate representation and are therefore undesirable. What the pseudopotential approach does is change the problem to reduce the size the basis set while trying to maintain all of the important physics.

For a single atom, the solution for the all electron (AE) form of the radial wavefunction, $R_{nl}^{AE}(r)$, satisfies the following equation Kohn–Sham equation:

$$\left\{ \frac{-1}{2} \frac{d^2}{dr^2} + \frac{l(l+1)}{2r^2} + V[\rho(r); r] \right\} r R_{nl}^{AE}(r) = \epsilon_{nl} r R_{nl}^{AE}(r), \quad (3.1)$$

where the bracketed terms correspond to the Kohn–Sham Hamiltonian. In this equation, the potential $V[\rho(r); r]$ is defined as

$$V[\rho(r); r] = \frac{-Z}{r} + V_H[\rho(r); r] + V_{xc}[\rho(r)], \quad (3.2)$$

where Z is the charge of the nucleus and V_{xc} is the exchange–correlation potential. What a pseudopotential does is to change the form of the radial wavefunction and the form of the Coulomb potential into an effective potential for the valence electrons of the atom. The wavefunction obtained under the pseudopotential used will be called

the pseudo-wavefunction $R_l^{PP}(r)$. The subscript n will be dropped because from now on we will only be concerned with the valence states.

We will be using generalized norm conserving pseudopotentials (GNCPs) [28, 29]. This class of pseudopotentials is bounded by a set of four rules. These rules will maintain almost all important physics of the problem while allowing one to modify the potentials and wavefunctions within a sphere in space for each component l of the valence wavefunctions. Even though the wavefunctions and potentials are different, the expectation values of important physical quantities are preserved. The four rules for constructing the GNCPs are the following:

1. The normality of the pseudo-wavefunction must be conserved for charge conservation,

$$\int_0^\infty |R_l^{AE}(r)|^2 4\pi r^2 dr = \int_0^\infty |R_l^{PP}(r)|^2 4\pi r^2 dr. \quad (3.3)$$

2. The all electron Kohn–Sham eigenvalues must be the same as the pseudo-eigenvalues

$$\epsilon_l^{AE} = \epsilon_l^{PP} \quad (3.4)$$

3. The pseudo-wavefunction must equal the all-electron wavefunction beyond a matching radius $r_{m,l}$; or at the least converges to the all-electron wavefunction very quickly; that is,

$$R_l^{AE}(r) = R_l^{PP}(r), \quad \text{for } r > r_{m,l} \quad (3.5)$$

4. Likewise, the pseudopotential must converge to the original Coulomb potential beyond some matching radius $r_{m,l}$,

$$V_l^{PP}(r) = \frac{-Z'}{r}, \quad \text{for } r > r_{m,l}, \quad (3.6)$$

where Z' is the screened nuclear charge.

As a consequence of the above conditions, the logarithmic derivatives of the pseudo and all-electron wavefunctions must be the same outside the radius $r_{m,l}$ at some energy ϵ that is not necessarily equal to the energy eigenvalue ϵ_i ; that is,

$$\frac{1}{R_l^{PP}(r, \epsilon)} \frac{d R_l^{PP}(r, \epsilon)}{dr} = \frac{1}{R_l^{AE}(r, \epsilon)} \frac{d R_l^{AE}(r, \epsilon)}{dr}. \quad (3.7)$$

The comparison of the logarithmic derivatives of the two solutions gives one an evaluation of the transferability of pseudopotential. This comparison can also be considered as a checking of the scattering properties of the pseudopotential. So far we have given a lot of emphasis to the pseudo-wavefunctions, not the pseudopotentials because the pseudopotentials are generated from the pseudo-wavefunctions.

The procedure for generating a pseudopotential from a pseudo wave function goes as follows. First, the screened pseudopotential, $V_{scr,l}^{PP}(r)$ is obtained by inverting Eq. (3.1) and solving for $V[\rho(r); r]$:

$$V_{scr,l}^{PP}(r) = \epsilon_l - \frac{l(l+1)}{2r^2} + \frac{1}{2rR_l^{PP}(r)} \frac{d^2}{dr^2} [rR_l^{PP}(r)]. \quad (3.8)$$

As a result we have a different potential for each angular momentum l . Once the screened pseudopotential is obtained, one can obtain the ionic pseudopotential by subtracting the Hartree and exchange-correlation potentials due to the valence electrons themselves,

$$V_{ion,l}^{PP}(r) = V_{scr,l}^{PP}(r) - V_H[\rho(r)', r] - V_{xc}[\rho(r)'], \quad (3.9)$$

where $\rho(r)'$ is the valence electron density. Once the ionic pseudopotential is obtained, we can replace the Coulomb potential $-Z/r$ with $V_{ion,l}^{PP}(r)$ in Eq. (3.2) and one obtains a different Hamiltonian for each angular momentum l . Finally we solve this Hamiltonian for the Kohn–Sham eigenfunction of the valence states with the modified potential.

To reduce the computational effort, Kleinman and Bylander (KB) proposed an operator representation of the pseudopotential [30]. The pseudopotential components can be written as

$$V_l^{PP}(r) = V_{local}^{PP}(r) + \sum_{l,m} \Delta V_l(r) |l, m\rangle \langle l, m|, \quad (3.10)$$

where

$$\Delta V_l(r) = V_{ion,l}^{PP}(r) - V_{local}^{PP}(r) \quad (3.11)$$

and $|l, m\rangle$ are the normalized spherical harmonics. Kleinman and Bylander replaced $\Delta V_l(r)$ with a projection operator,

$$\Delta V_l(r) = E_L^{KB} |\zeta_l\rangle \langle \zeta_l|, \quad (3.12)$$

where

$$|\zeta_l\rangle = \frac{\Delta V_l(r) R_l^{PP}(r)}{\langle R_l^{PP} | \Delta V_l^2 | R_l^{PP} \rangle^{1/2}} \quad (3.13)$$

and

$$E_l^{KB} = \frac{\langle R_l^{PP} | \Delta V_l(r)^2 | R_l^{PP} \rangle}{\langle R_l^{PP} | \Delta V_l(r) | R_l^{PP} \rangle}. \quad (3.14)$$

This procedure reduces the computational demand of the density functional calculations involving the nonlocal potential energy matrix elements.

3.1 Ghost State Analysis

One problem that arises from the operator representation is the appearance of ghost states. First we will define the KB Hamiltonian to be the Hamiltonian of Eq. (3.1) except that we will use the pseudopotential in the KB representation described earlier. Because of the form of the KB Hamiltonian, it does not obey the Wronskian theorem. This theorem implies that eigenfunctions are ordered such that the energy increases with the number of nodes. As a result, it is possible that the KB Hamiltonian can have eigenfunctions that contain nodes that are lower in energy than the zero-node eigenfunction. These unphysical states are termed as ‘‘Ghost States’’. Because of this property, one must be careful in the pseudopotential generation process [31].

Gonze found the way to determine if a ghost state was present by analyzing two quantities [32]. The first is the KB energy defined in Eq. (3.14). The second is the KB cosine energy

$$C_l^{KB} = \frac{\Delta V_l^{rms}}{E_l^{KB}}, \quad (3.15)$$

where

$$\Delta V_l^{rms} = \langle R_l^{PP} | \Delta V_l(r) | R_l^{PP} \rangle \quad (3.16)$$

By examining these two quantities as a function of the matching radii $r_{m,l}$ for different l , one can eliminate the ghost states. These ghost states can also be eliminated or avoided by choosing the proper angular momentum component for the local potential.

3.2 Pseudo-wavefunction Construction

There are many ways to modify the core region of the valence wavefunctions that follow the rules of the GNCPP. The first was done by Hamann, where gaussian type pseudo-wavefunction converges to the valence wavefunction near the matching radius [28]. A few years later, Troullier and Martins proposed a new construction that exactly matches the wavefunction and the wavefunction derivative at the matching radius [29]. The functional form of the pseudo-wavefunction in the Troullier Martins type is a Taylor series in r . The last is the Vanderbilt form of the pseudopotentials which that is softer than the TM and Hamann types [33]. The benefit of the Vander-

bilt type is that the potentials are smoother, but they are also less reliable than the Troullier Martins or the Hamann type. The general rule is use a construction that provides a soft pseudopotential but also has good transferability for the targeted system.

3.3 Nonlinear Core-Valence Corrections

In general, the above pseudopotential scheme works very well for most systems, but not for all. Our main assumption is that there is a very weak coupling between the core and valence electrons of the atom. In cases where the coupling is stronger, one can begin by correcting the exchange-correlation energy. From Eq. (3.9), one can see that only the exchange-correlation energy of the valence charge is subtracted. In cases where the coupling is strong, there will be a nonlinear dependence of the exchange-correlation energy on the total charge density. This property greatly reduces the transferability of the pseudopotential. In 1982, Louie *et. al.* proposed that the exchange-correlation energy of *both* the valence and core regions should be subtracted

$$V_{ion,l}^{PP}(r) = V_{scr,l}^{PP}(r) - V_H[\rho(r)', r] - V_{xc}[\rho^c(r) + \rho(r)'], \quad (3.17)$$

where $\rho^c(r)$ is the core charge density.

At first glance, this may seem to be a very simple idea, but it is not that straightforward. As mentioned earlier, the core density is highly oscillatory and undesirable when using a plane wave basis due to the fact that the oscillations require many

plane waves. The second issue is that any error in the valence density will be greatly enhanced when added to the core density. The valence density is usually solved iteratively and the inclusion of the true core density in the above equation will increase the number of iterations required to attain convergence. The solution is to introduce a model core that is small where the core density is high. In the region where the core density is high, the valence density will be low so the effects in that region will be small. Near the point where the core and valence densities are close to the same magnitude, the model density should converge to the true core density $\rho^c(r)$. One form for the model density is

$$\rho_{model}(r) = \begin{cases} A \sin(Br)/r, & \text{for } r \leq r_{nlcv} \\ \rho^c(r), & \text{otherwise,} \end{cases} \quad (3.18)$$

where A and B are determined by $\rho^c(r_{nlcv})$ and $\frac{\partial}{\partial r}\rho^c(r)|_{r_{nlcv}}$. The parameter r_{nlcv} is usually chosen the radius at which the model core matches the true core density. In general this correction is needed when the exchange-correlation energy is important. For example the exchange-correlation energy is a major contributor to the binding energy in alkali metals.

CHAPTER 4

COMPUTATIONAL DETAILS

In the previous chapters, the details about the method and theory have been discussed. Now we turn to the aspect regarding their computational implementation. For the calculations presented here, we have used various versions of the fhi98md code [35] ported to different machines. This package has been in development for many years and is very current with the newest schemes for the iterative minimization of the total energy. It also implements the latest approximations for the exchange-correlation energy. One version has been ported over to the Cray T3E platform by the developers and we have also spent much time parallelizing the serial version for our own SGI Power Challenge systems.

There are many details that are involved in implementing density functional theory computationally. In the next few sections, I will address the most relevant issues.

4.1 Basis Functions

In the preceding chapter, it was mentioned that planewaves would be used as the basis set for our calculations. There are many advantages to using planewaves:

- Efficient Fourier transform algorithms exist for the transformations to and from k -space.
- There are no Pulay forces. These are forces arising from a basis set that is dependent on the coordinates of the nuclei.
- \mathbf{r} and \mathbf{p} operators are simple operations on plane waves.
- Matching conditions at the boundaries are easily handled with Bloch states.

There is only one disadvantage using a planewave basis set:

- Localized orbitals and pure Coulomb potentials require a large number of planewaves to obtain good resolution.

This disadvantage means that to resolve real atomic systems, we will need a large basis set. As the size of the basis set increases, so do the computational resources required to do the calculation.

4.2 Basis Representation

For calculations of bulk properties, one must use periodic boundary conditions to approximate an infinite system. To treat the periodic behavior of the ionic potential of the crystal, the Bloch states are constructed for our basis set. Bloch states are still manageable because of their planewave form.

A crystal is defined as a structure composed of repeated units [36]. This repetition of atoms defines a periodicity in the ionic potential,

$$V(\mathbf{r}) = V(\mathbf{r} + \mathbf{T}), \quad (4.1)$$

where \mathbf{T} is defined as a translational vector of the crystal and defined as

$$\mathbf{T} = n_1 \mathbf{a}_1 + n_2 \mathbf{a}_2 + n_3 \mathbf{a}_3 \quad (4.2)$$

with \mathbf{a}_i being the lattice unit vectors and the arbitrary n_i integers. One would expect the electron density to have the same periodicity,

$$n(\mathbf{r}) = n(\mathbf{r} + \mathbf{T}), \quad (4.3)$$

which is constructed from the occupied states,

$$n(\mathbf{r}) = \sum_i \phi_i(\mathbf{r}) \phi_i^*(\mathbf{r}). \quad (4.4)$$

Bloch proved that the solution for the periodic potential must take the form

$$\phi_{i,\mathbf{k}}(\mathbf{r}) = \exp(i\mathbf{k} \cdot \mathbf{r}) u_{i,\mathbf{k}}(\mathbf{r}), \quad (4.5)$$

with

$$u_{i,\mathbf{k}}(\mathbf{r}) = u_{i,\mathbf{k}}(\mathbf{r} + \mathbf{T}). \quad (4.6)$$

From the definition for $u_{i,\mathbf{k}}$ in Eq. (4.6), one can see that using planewaves of the form $\exp(i\mathbf{G} \cdot \mathbf{r})$ will satisfy the periodicity condition if \mathbf{G} is a reciprocal lattice vector of the form

$$\mathbf{G} = m_1 \mathbf{b}_1 + m_2 \mathbf{b}_2 + m_3 \mathbf{b}_3, \quad (4.7)$$

where the m_i are arbitrary integers and \mathbf{b}_j are the reciprocal lattice unit vectors satisfy the condition

$$\mathbf{a}_i \cdot \mathbf{b}_j = 2\pi \delta_{i,j}. \quad (4.8)$$

So we have

$$\mathbf{G} \cdot \mathbf{T} = \sum_i \sum_j n_i m_j \mathbf{a}_i \cdot \mathbf{b}_j = \sum_i n_i m_i 2\pi. \quad (4.9)$$

The Bloch states, $\phi_{i,\vec{\mathbf{k}}}$ can be written as

$$\phi_{i,\mathbf{k}}(\mathbf{r}) = \sum_{\mathbf{G}} c_{\mathbf{G},\mathbf{k}} \exp [i(\mathbf{G} + \mathbf{k}) \cdot \mathbf{r}] \quad (4.10)$$

In most applications, the set of \mathbf{G} vectors is determined by an energy cutoff. All vectors $(\mathbf{G} + \mathbf{k})$ with energy $\frac{1}{2}|(\mathbf{G} + \mathbf{k})|^2$ less than the energy cutoff are used in the basis.

4.3 Electronic Temperature

It has been shown that one can introduce a temperature into the electronic states by using partial occupancies of the Kohn–Sham orbitals. To include the finite temperature one modifies the previous definition of the electron density with

$$n(\mathbf{r}) = \int \sum_i f_{i,\mathbf{k}} |\phi_{i,\mathbf{k}}(\mathbf{r})|^2 d\mathbf{k} \quad (4.11)$$

where the $f_{i,\mathbf{k}}$ is the Fermi distribution function given by

$$f_{i,\mathbf{k}} = \frac{1}{\exp(\beta(\epsilon_{i,\mathbf{k}} - \epsilon_f)) + 1} \quad (4.12)$$

where $\beta = 1/k_B T$, with k_B is the Boltzmann constant, T the temperature, and ϵ_f is the Fermi energy. Although this might seem straight forward, it is not. One must remember that the Kohn–Sham eigenvalues are not the true eigenenergies of the system: they are the derivatives of the total energy with respect to the appropriate occupation number. The generalization of the finite temperature scheme was first introduced by Mermin in 1965 [37].

This finite temperature scheme is very important for metallic systems. During the iterative scheme, ϵ_f is constrained by the total number of valence electrons,

$$N_e = \sum_i \int f_{i,\mathbf{k}} d\mathbf{k}. \quad (4.13)$$

Under the finite temperature distribution, one has one more degree of freedom for to work on during the iterations in the matrix diagonalization (see Section 2.7). Not only will the planewave expansion coefficients be changed, but also the Fermi energy ϵ_F and the occupation numbers $f_{i,\mathbf{k}}$. This slows down the rate of convergence but allows for partial occupancies of the Kohn–Sham eigenstates.

For semiconducting and insulating systems, there is no occupancy at the Fermi level. This means that the occupation numbers $f_{i,\mathbf{k}}$ are either 1 or 0. In metals, this is not the case and there many states at the Fermi level. Therefore without the smooth Fermi distribution function, states near the Fermi surface would have a discontinuous change in occupation number, which may not allow the system to reach the ground state. By introducing a temperature in the distribution, the occupation number of the states near the Fermi level will not change discontinuously.

4.4 Finite k-Space

In the previous section, a dependence of the eigenstates, eigenvalues and occupation numbers are all dependent on the Bloch wavevector \mathbf{k} . The electron density must be integrated over the first Brillouin zone. The first Brillouin zone is defined to be the Wigner-Seitz primitive cell of the reciprocal lattice [36]. The reciprocal lattice is defined by the \mathbf{b}_i mentioned in Eq. (4.7). A numerical integration through out the entire Brillouin Zone is an enormous task. It has been shown that the integration above can be done over a small selection of highly symmetric points in the Brillouin

Zone [38, 39]. This reduces the integral to a summation over the symmetric \mathbf{k} points

$$n(\mathbf{r}) = \sum_{\mathbf{k}} \sum_i w_{\mathbf{k}} f_{i,\mathbf{k}} |\phi_{i,\mathbf{k}}(\mathbf{r})|^2 \quad (4.14)$$

with the condition that

$$\sum_{\mathbf{k}} w_{\mathbf{k}} = 1. \quad (4.15)$$

CHAPTER 5

RUBIDIUM PART I

In this chapter, the process of constructing a good pseudopotential for rubidium will be addressed. In Chapter 3, the fundamental ideas behind the pseudopotential were discussed and we will use them here to generate a pseudopotential for rubidium. For the next few sections, we will be testing different pseudopotentials and different approximations for the exchange-correlation energy to see how these approximations affects the calculated properties of rubidium

5.1 Pseudopotential Construction

There many choices one can make to construct a good quality pseudopotential. A good pseudopotential:

- has good transferability (The logarithmic derivatives match well);
- is soft (few planewaves are needed to describe the potential) ;
- has no ghost states (see Section 3.1).

Here is a list of the choices one can make in the pseudopotential approximation:

1. The approximation for the exchange-correlation potential;

2. The matching radii for each of the nonlocal components of the pseudopotential ($r_{m,l}$);
3. The radius for the nonlinear core valence correction (if needed);
4. The Hamann or Troullier–Martins form of the pseudopotential;
5. The choice of the local component of the pseudopotential in the Kleinman–Bylander representation;
6. Partial occupancies of the valence orbitals.

The first item on the list is the approximation for the exchange-correlation potential. As discussed in Chapter 2, this one of the few approximations we have made in density functional theory. There are basically two choices for this approximation. One is the local density approximation (LDA) which approximates the exchange-correlation potential of the electron density as if it were a homogenous electron gas (see Section 2.6). Here the exchange-correlation potential is dependent on only the local electron density, $n(\mathbf{r})$ at some point \mathbf{r} in space. This the most basic and most accepted approximation for the exchange-correlation energy.

The second choice for the approximation to the exchange-correlation energy is the generalized gradient approximation (GGA) which is dependent not only the electron density, $n(\mathbf{r})$ at some point \mathbf{r} , but also the magnitude of the gradient of the electron density, $|\vec{\nabla}n(\mathbf{r})|$. Usually, the GGA works better because it contains both the zeroth and first order terms in a Taylor expansion of the electron density. One

problem arises in the potential related to a term that is proportional to $|1/\vec{\nabla}n(\mathbf{r})|$. In cases where this term is small, instabilities may arise in the calculations. In general, one cannot foresee which approximation will work and one compare the results for both approximations with experimental data.

The second item on the list is the proper choice of the matching radius where one matches the modified core of the atom to the true valence wavefunction. This radius also pertains to the radius where each of the core potentials is matched to the screened Coulomb potential. This radius is usually chosen as the outermost maximum of the particular wavefunction and can be different each l . In some cases, the radii can be modified to remove ghost states, if they exist.

The third item on the list is not always necessary, except where exchange-correlation effects are critical. The nonlinear core valence correction is an approximation used to correct the exchange-correlation effects between the core and the valence electrons of the atom. This radius is chosen where the valence and core densities are equal.

The fourth item is the choice for the actual construction of the core region of the pseudo-wavefunction. The choice between the two forms is usually a personal preference. These were referred to in Section 3.2. Sometimes one of the forms is more transferable and/or softer than the other. The reason the Vanderbilt form was not listed was due to the fact that it is somewhat nonuniversal and less predictable.

The fifth item on the list is the choice for the local component of the pseudopotential. For the Kleinman–Bylander representation of the pseudopotential, we need to assign one of the components as local. Usually this is also a preference, but in certain cases, the choice of the local component can be made to avoid ghost states, if they are present.

The final item on the list has to do with the partial occupancies of the valence orbitals. This is done by moving some electrons from the lowest-energy configuration to a higher-energy configuration. This improves the pseudopotential transferability because the higher-energy configuration imposed may be closer to the environment the pseudopotential will be placed in.

As one can see, in practice, the construction of the pseudopotential can be quite complicated. Knowledge about all of the previous choices for the pseudopotential approximation can aid in generating the best pseudopotential.

5.2 The Pseudopotential Program

The package we used to generate all of the following pseudopotentials and graphs is called fhi98PP [40]. The package was written by Dr. Martin Fuchs and distributed for free by the Fritz–Haber Institute. The program is written in Fortran77 and comes with all of the tools to modify and analyze a pseudopotential. Some modifications to this program were made to allow for more extreme modifications to the pseudopotentials than are normally done.

5.3 Pseudopotential Construction in Practice

The construction of the pseudopotential for rubidium will be analyzed in great detail here. We will begin by constructing a pseudopotential for rubidium. These calculations were done using the LDA for the exchange-correlation potential and the pseudopotentials were constructed within the Troullier–Martins scheme [29]. The matching radii for $l = 0, 1, 2$ are chosen to be $r_{m,l} = 4.20, 4.60, 3.2 a_0$.

We begin the analysis with the all-electron calculations for rubidium. These are the calculations that are done to find the true wavefunctions that are needed to generate the pseudopotentials. The first test that is done is the calculation of the ionization energy. This is the difference between the ground-state energy of the neutral atom and the ground state energy of the ion. This difference is 0.15707 Hartree, which is very close to the experimental value of 0.15350 Hartree.

5.4 Transferability and Occupancies

Based on the work of McMahan [13] we expect to see some d characteristics in our pseudopotential. Therefore, the pseudopotential was generated with the valence configuration $5s^{0.8}5p^{0.1}4d^{0.1}$. In Fig. 5.1 and Fig. 5.2 we show the $l = 0, 1, 2$ components of the pseudopotentials and the valence pseudo-wavefunctions, respectively. The LDA was used for the exchange-correlation potential and the $l = 2$ component is used as the local component for the KB representation.

In Fig.5.1, both the pseudo-wavefunctions and pseudopotentials are shown. One

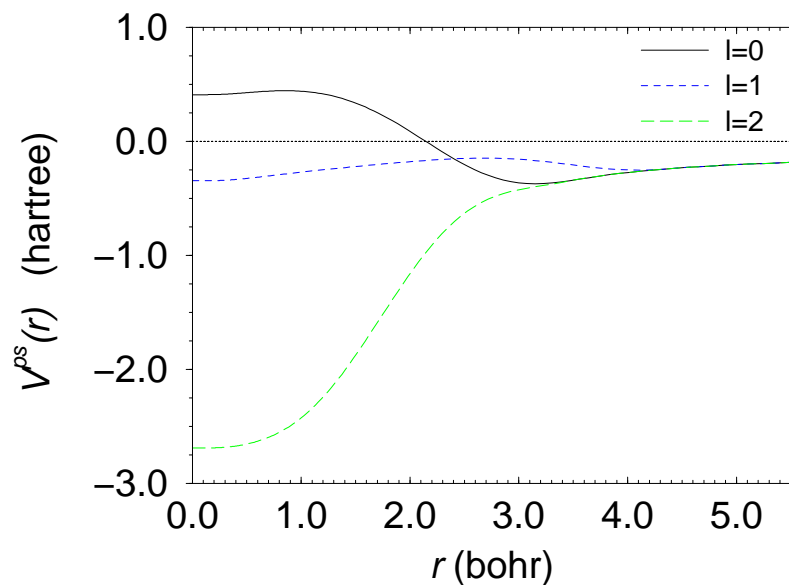


Figure 5.1: Components of the pseudopotential for rubidium for the $l = 0, 1, 2$ components.

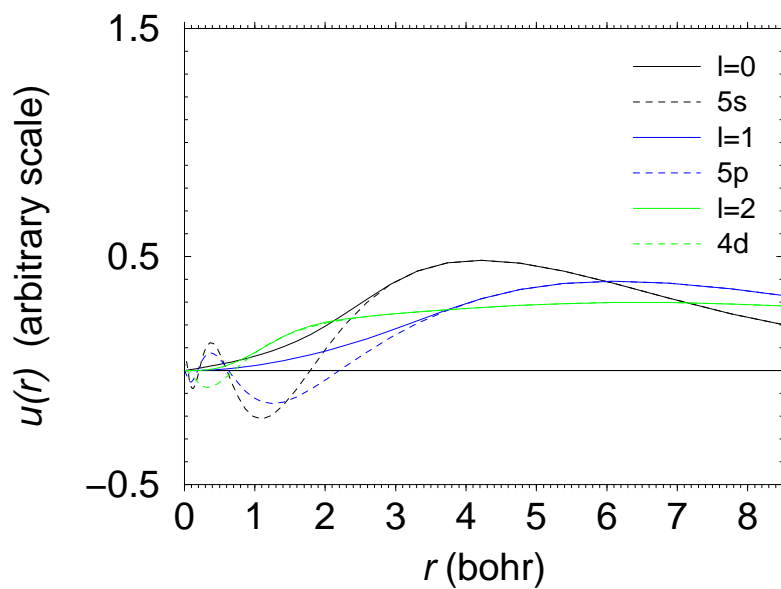


Figure 5.2: This is a plot of the $l = 0, 1, 2$ components of the pseudo-wavefunction for rubidium. The smooth curves are the pseudo-wavefunctions, whereas the dashed curves are the all-electron solutions.

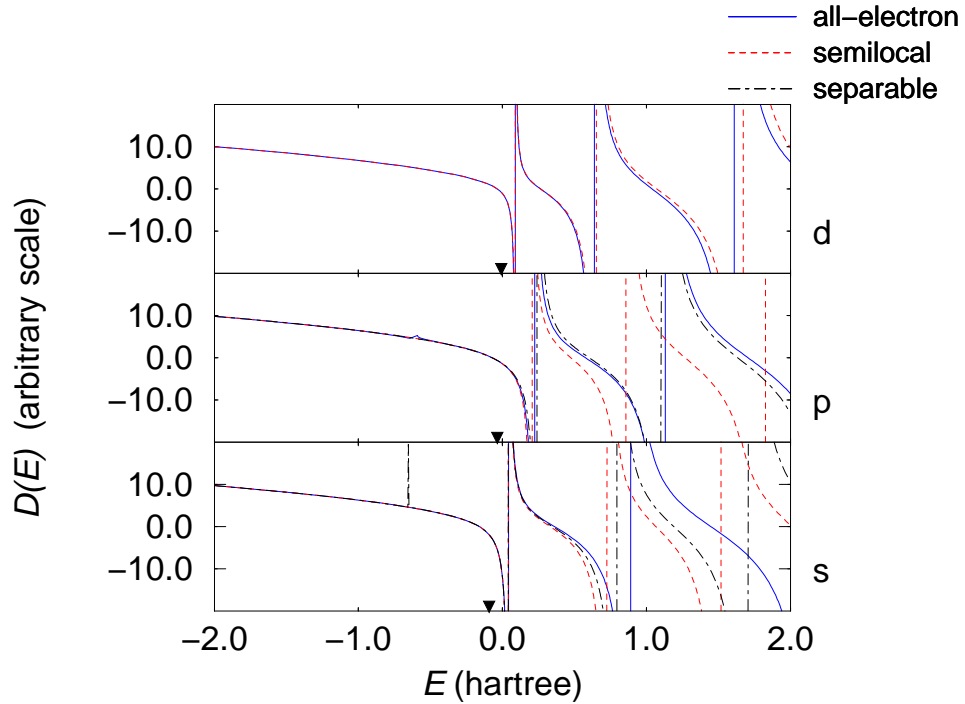


Figure 5.3: The logarithmic derivatives $D(E)$ of all the $l = 0, 1, 2$ components of the pseudopotential for rubidium. The peak deep in energy in the s channel is a ghost state.

can see that the pseudopotentials are quite soft by the energy scale for each of the components. Each of the components is quite smooth and behaves quite nicely beyond each of the matching radii. Now that we have a smooth pseudopotential and we can now look at transferability. The logarithmic derivatives for this pseudopotential are shown in Fig. 5.3.

As stated earlier, the transferability test involves analyzing the logarithmic derivatives of our pseudo-wavefunctions to see if they match the all-electron solutions. One can see that the semilocal, KB, and all-electron logarithmic derivatives agree well. Each time $D_l(E)$ crosses the zero point on the y axis corresponds to an

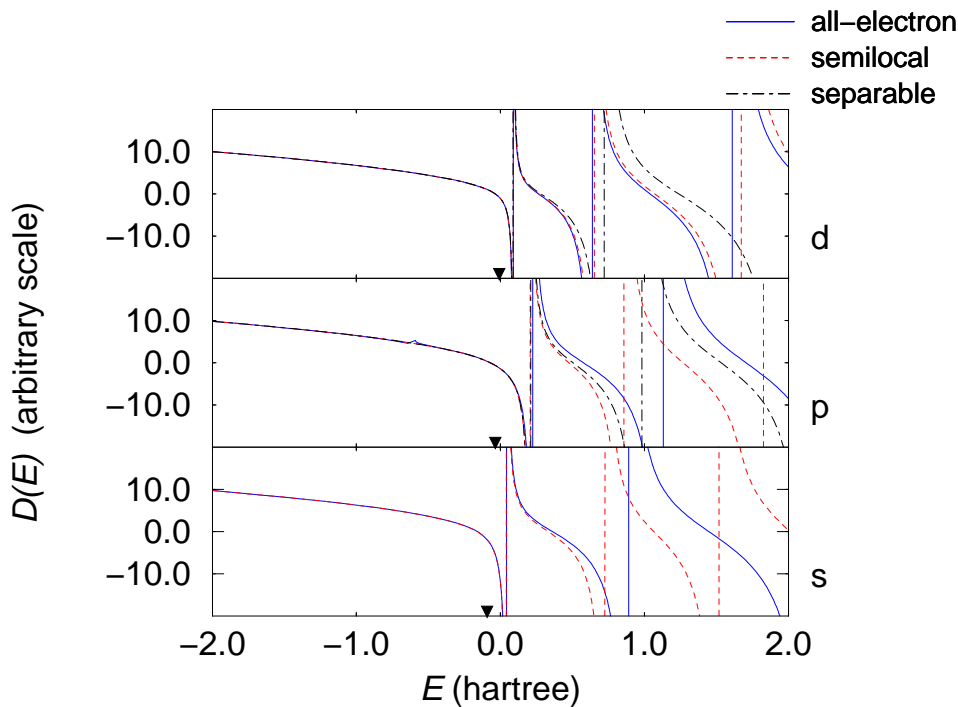


Figure 5.4: This is a plot of the logarithmic derivatives $D(E)$ of each of the $l = 0, 1, 2$ components of the pseudopotential for rubidium. Here the $l = 0$ component is used as the local component and the ghost state in Figure 5.3 is removed.

eigenvalue. The energies on the horizontal axis are shifted arbitrarily. Note that in the $l = 0$, channel there are crossings in the KB form of the pseudopotential but not in the semilocal or all-electron forms. This is a ghost state that must be removed. If we change the choice of the local component from $l = 2$ to $l = 0$ one can remove the ghoststate as seen in Fig.5.4.

5.5 Further Testing

Up to this point, we have done as much as possible from the pseudopotential end. The next thing one can do is to see how large a basis set must be and how many

E_{cut} (Ry)	Total Energy (eV/atom)
5	-5.19031
10	-5.21967
15	-5.22386

Table 5.1: The difference in ground-state energy for three different values for the energy cutoff is shown. One can estimate that with an energy cutoff of 10 Rydbergs, the energy converges to a difference of about 5 meV.

number of k -points	Total Energy (eV/atom)
6	-5.20348
26	-5.22993
68	-5.22386

Table 5.2: The difference in total energy for increasing the number of k -points in the first BZ. One can estimate that with 26 k -points converges to a difference of about 10 meV.

k -points are needed to converge the total energy. The k -point set is generated using the Monkhorst Pack scheme mentioned in Chapter 4, and the electronic temperature of the Fermi distribution is set to 300K which is approximately 25 meV. In Table 5.1 the ground state energy for the bcc structure of rubidium is calculated for different values for the energy cutoff. Again, this energy cutoff determines the size of the basis set. These energies were calculated for a volume of $500 a_0^3/\text{atom}$ and with 182 k -points in the first BZ. Table 5.1 shows that for an energy cutoff of 10 Rydbergs, we can have the energy converge to a difference of 5 meV. We can also check the convergence versus the number of k -points used.

In Table 5.2, the ground-state energy for different numbers of k -points in the first BZ are given. These energies were calculated for a volume of $500 a_0^3/\text{atom}$ with

Number of k -points	Ecut (Ry)	E_0 (eV)	V_0 (a_0)	B_0 (GPa)	B'_0
6	5	-6.7300	482.4	4.71	2.34
6	10	-6.0729	464.9	3.18	2.57
6	15	-5.8711	459.3	3.32	3.13
26	5	-5.4641	479.2	3.31	6.48
26	10	-5.8147	456.1	3.37	3.43
26	15	-5.9168	452.0	3.43	3.11
68	5	-5.5333	483.9	3.34	5.37
68	10	-5.9156	460.3	3.33	3.05
68	15	-6.0811	456.0	3.35	2.66
Experiment 1 [42]			589.4	2.92	4.1
Theory 1 [9]			540	3.5	3.9
Experiment 2 [43]			588.4	2.6	
Theory 2 [11]			519.6	4.2	4.1

Table 5.3: The fitted parameters to the Murnaghan equation of state are given for different energy cutoff values and different numbers of k -points.

an energy cutoff of 15 Rydbergs. One can estimate that for 26 k -points we can the energy to a difference of 10 meV. It should be noted that in metallic systems, one needs a large number of k -points to converge not only the total energy, but also the Fermi energy. This is why in some cases the energy will fluctuate slightly higher when the number of k -points is increased.

Now we will put our pseudopotentials in use in a series of bulk calculations to test suitable values for the energy cutoff and the number of k -points to be used. We begin by doing a series of energy versus volume calculations for different k -point sets and different values for the energy cutoff. The energy is calculated at 20 a_0^3 /atom intervals starting from 380 a_0^3 /atom. We will test the convergence by doing a nonlinear fit to 7 data points centered around the volume that gives the

minimum energy. In Table 5.3, the fitted parameters of the Murnaghan equation of state are listed. The Murnaghan equation of state is defined as [41]

$$E = \frac{B_0 V}{B'_0} \left(\frac{1}{B'_0 - 1} \left(\frac{V_0}{V} \right)^{B'_0} + 1 \right) + E_0, \quad (5.1)$$

where E_0 is the Energy at the equilibrium volume V_0 , B_0 is the bulk modulus at the equilibrium volume and $B'_0 = \partial B_0 / \partial P$. In Table 5.3, the convergence to specific values for E_0 and B'_0 is not very good, but is better for B_0 and V_0 . One should also note that B_0 is larger than the experimental value and less than other theoretical values. On the other hand V_0 , is smaller than both the experimental and theoretical results. This is typical in LDA to underestimate equilibrium volumes and lattice constants.

As mentioned in Section 3.3, the exchange-correlation energy is very important in alkali metals. Here we perform the same test except include the nonlinear core valence correction of Louie *et. al.* [34]. In Fig. 5.5 we plot the core, valence, and model core electron densities for a single rubidium atom. The radius at which the densities are the same is at $r = 3.5a_0$, the radius chosen for the model core. In Table 5.4, the results for the same tests as done in Table 5.3 are given. The results show less variance with a larger k -point sets and the larger energy cutoff. The values tend to agree more with the theoretical calculations which is expected since the other calculations also use the LDA. One last thing to check is how the fitted parameters vary with the valence configuration under which they are generated. In Table 5.5,

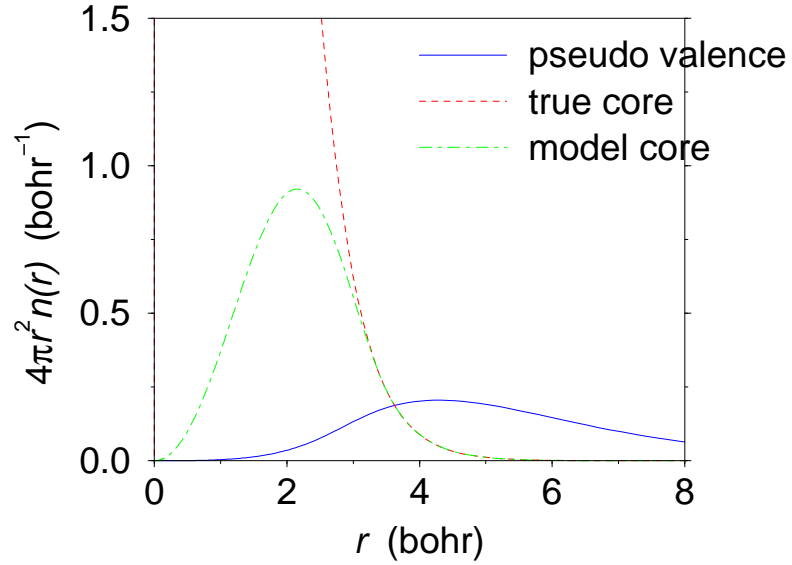


Figure 5.5: The core, valence, and model core densities for the pseudopotential of Rb. The model core radius for the nonlinear core valence correction is $3.5a_0$.

Number of k -points	Ecut (Ry)	E_0 (eV)	V_0 (a_0)	B_0 (GPa)	B'_0
6	5	-16.870	540.0	3.30	5.34
6	10	-17.049	524.6	3.65	4.32
6	15	-17.155	522.4	3.56	3.70
26	5	-18.377	537.7	3.56	1.95
26	10	-17.244	519.0	3.70	3.52
26	15	-17.184	515.9	3.64	3.71
68	5	-17.741	539.2	3.43	2.39
68	10	-17.235	521.7	3.73	3.55
68	15	-17.181	518.8	3.62	3.70
Experiment 1 [42]			589.4	2.92	4.1
Theory 1 [9]			540.0	3.5	3.9
Experiment 2 [43]			588.4	2.6	
Theory 2 [11]			519.6	4.2	4.1

Table 5.4: The fitted parameters to the Murnaghan equation of state are give for different energy cutoff values and numbers of k -points usin the nonlinear core valence correction.

Valence Occ.	nlcv	E_0 (eV)	V_0 (a_0)	B_0 (GPa)	B'_0
$5s^{0.8}5p^{0.1}4d^{0.1}$	no	-5.8147	456.1	3.37	3.43
$5s^{0.1}5p^{0.1}4d^{0.8}$	no	-6.2235	409.2	3.99	2.78
$5s^{0.5}5p^{0.1}4d^{0.1}$	yes	-17.244	519.0	3.70	3.52
$5s^{0.1}5p^{0.1}4d^{0.8}$	yes	-17.170	520.1	3.70	3.59

Table 5.5: The fitted Murnaghan parameters among pseudopotentials with the nonlinear core valence correction and pseudopotentials generated with different valence configurations. The nonlinear core valence correction improves transferability significantly.

we show the results for the fitted parameters to the Murnaghan equation of state are given for a pseudopotential that was generated using a valence configuration of $5s^{0.1}5p^{0.1}4d^{0.8}$.

The results show that the pseudopotential is highly transferable when the nonlinear core valence correction is used. The equilibrium volume is a little too small as are the other values. It should be noted that the decrease in E_0 , when using the nonlinear core valence correction, is due to inclusion of the exchange-correlation energy of the core. Without the correction, this contribution to the energy is not included in the pseudopotential. Now let us see how well we can calculate the bcc to fcc phase transition. In Fig.5.6, one can see the energy curves for both structures. These calculations were done using the good pseudopotential for 26 k -points and an energy cutoff of 10 Rydbergs. As one can see the energies for the two structures are very similar. In Fig. 5.7 we plot the energy of the bcc structure with respect to the fcc structure. One can see in this figure that the fcc structure is lower in energy for volumes less than $270 a_0^3/\text{atom}$. This transition volume for the bcc to fcc transition

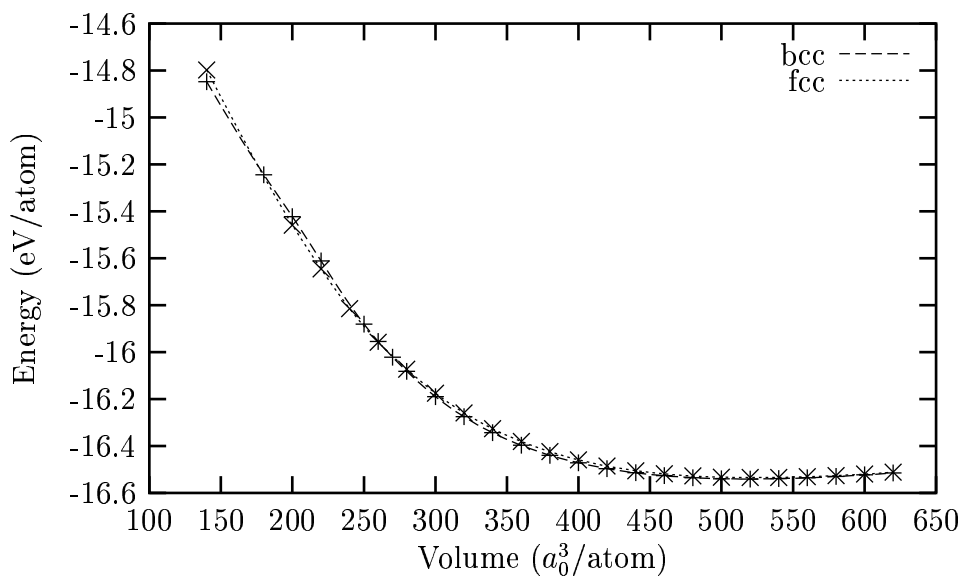


Figure 5.6: This is a plot of the energy-volume curves for the fcc and bcc structures. The first volume at which they cross is $270 a_0^3/\text{atom}$. Fits through the data points are done with cubic splines.

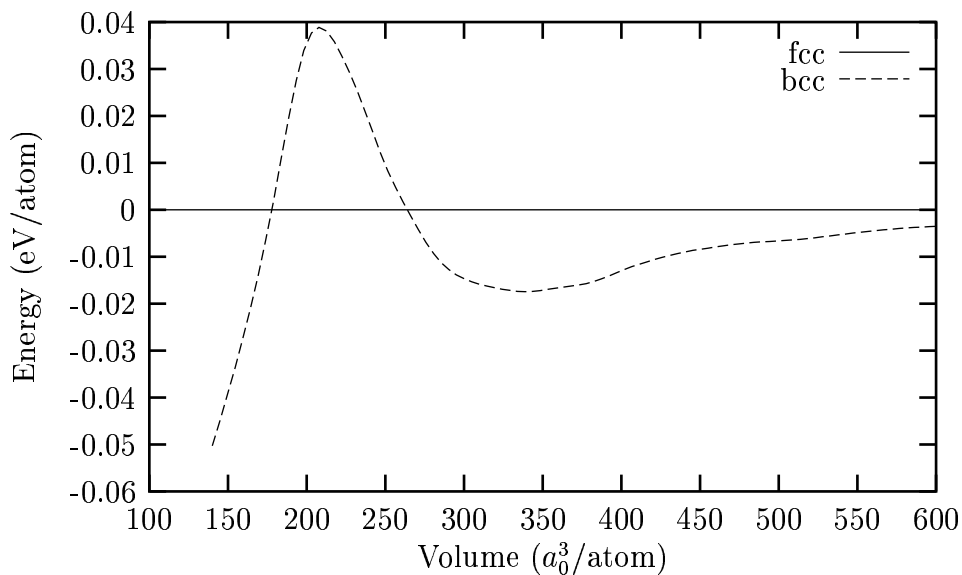


Figure 5.7: Energy-volume curves for the fcc and bcc structures. In this figure the fcc curve is used as the reference energy. The first volume at which they cross is $270 a_0^3/\text{atom}$. Fits through the data points are done with cubic splines.

which is slightly less than the theoretical value of $300a_0^3/\text{atom}$ obtained by Louie *et al.* [9]. The experimentally observed transition volume is $300a_0^3/\text{atom}$ [4]. To find the pressure for the bcc to fcc transition one must plot the enthalpy versus pressure. Under pressure induced transitions it is the enthalpy that is the conserved quantity. The enthalpy is given by

$$H = E + PV \quad (5.2)$$

or

$$dH = VdP + TdS. \quad (5.3)$$

where E is the total energy, P is the pressure, V is the volume, T is the temperature, and S is the entropy of the system. In Fig. 5.8 the enthalpies of the two structures are compared and one obtains a from the bcc phase to the fcc phase at 7 GPa, as observed in experiment [2].

5.6 The PBE Approximation

We will now use one of the GGA approximations for the exchange-correlation potential introduced by Perdew, Burke, and Ernzerhof [44]. To begin we carry out the same tests as before. The pseudopotential has the same matching radii and radius for the nonlinear core correction as the previous potentials except now the PBE approximation has been used for the exchange-correlation energy potential. With this approximation we get much better agreement with the experimental values. One

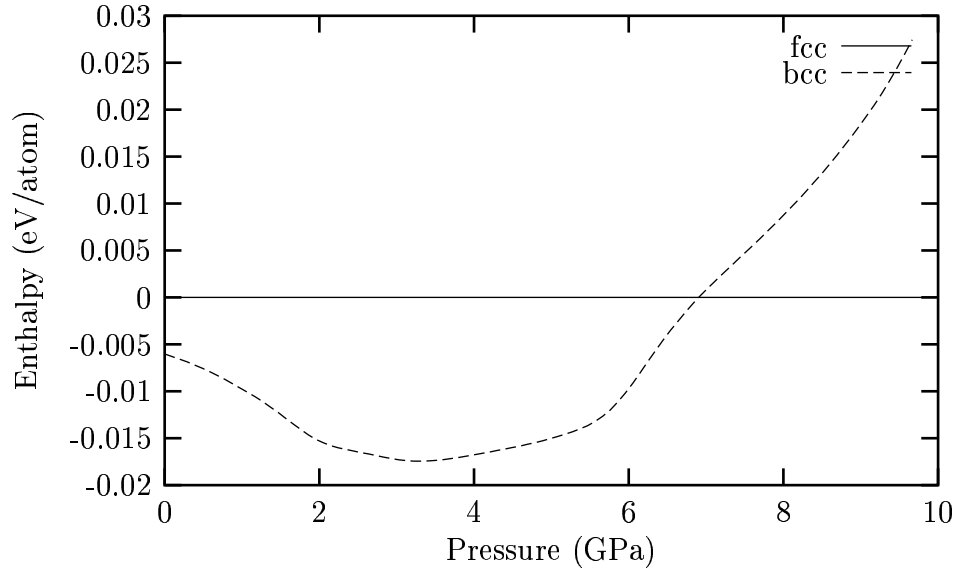


Figure 5.8: Enthalpy-pressure curves for the bcc structure in comparison to that of the fcc curve. The transition from the bcc to the fcc structure is at 7 GPa, which is the same as as the experimental value. Fits through the data points are done with cubic splines.

Ecut (Ry)	Number of k -points	E_0 (eV)	V_0 (a_0)	B_0 (GPa)	B'
5	26	-13.2372	609	2.6	6.95
10	26	-13.6629	600	2.79	3.47
15	26	-13.6348	600	2.78	3.44
5	68	-13.2965	612	2.71	5.87
10	68	-13.6481	603	2.80	3.41
15	68	-13.6360	602	2.80	3.44
exp 1 [42]			589.4	2.92	4.1
theory 1 [9]			540	3.5	3.9
exp 2 [43]			588.4	2.6	
theory 2 [11]			519.6	4.2	4.1

Table 5.6: The fitted parameters to the Murnaghan Equation of state are give for different energy cutoff and different numbers of k -points with the nonlinear core valence correction and the PBE approximation for the exchange-correlation potential.

Valence Occ.	nlev	E_0 (eV)	V_0 (a_0)	B_0 (GPa)	B'
$5s^{0.8}5p^{0.1}4d^{0.1}$	no	-5.3580	635	2.29	3.41
$5s^{0.1}5p^{0.1}4d^{0.8}$	no	-5.5017	571	2.52	3.40
$5s^{0.8}5p^{0.1}4d^{0.1}$	yes	-13.6629	600	2.79	3.47
$5s^{0.1}5p^{0.1}4d^{0.8}$	yes	-13.5809	591	2.82	3.49

Table 5.7: Above the fitted parameters to the Murnaghan equation of state are give for different energy cutoff values and different folding parameters.

can also check the transferability of the pseudopotential and those results are given in Table 5.7.

5.7 Discussion

We have demonstrated that using density functional calculations can obtain good theoretical results for the properties of rubidium at low pressure. Even with the LDA underestimating the equilibrium volume of the bcc structure by about 10%, we still obtained the correct pressure for the bcc to fcc transition. This pseudopotential at higher pressures fails due to overlap with the $4s$ and $4p$ states that were treated as part of the inert core. In the next chapter, we will generate a new pseudopotential that is more suitable for higher pressure to study the complex structures of rubidium observed in recent experiments [2, 3, 4].

CHAPTER 6

RUBIDIUM PART II

As stated at the end of the preceding chapter, the one valence electron approximation in the pseudopotential for rubidium fails as the volume gets too small. Other pseudopotentials with different matching radii failed much worse than the pseudopotentials used in the preceding chapter. Because it is the Coulomb repulsion between the core electrons that causes the energy to rise under compression, one must assume that it is the approximation of the core that is at fault. Let us attempt now to approximate the core better by treating the core states $4s$ and $4p$ on equal footing with the valence electron.

We begin by generating a pseudopotential with the following valence configuration: $4s^2 4p^6 4d^1$. We have also used a small nonlinear core valence correction to take into account any possible exchange-correlation energy issues of the deep $3d$ level. During the construction of this pseudopotential, some problems arose. We observed that if there was any occupancy of the valence $5s$ or $5p$ orbital, a singularity at the origin in the components of the pseudopotential occurred. We believe that this is an artifact due to the way that the charge at $r = 0$ is calibrated with the charge at infinite distance. In the pseudopotential program, there is a parameter to remove

the charge at infinity which is specified by some large radius. Although we could not correct the problem by increasing this parameter, we could introduce such a singularity in other pseudopotentials by reducing the parameter. For now we should be aware of this issue in the approximation.

There are other issues to be dealt with, including the instability of the PBE functional. During both the pseudopotential generation and the electronic structure calculations, convergence was very slow and sometimes unstable. Therefore, for the calculations here the LDA for the exchange-correlation energy is used.

The calculated energies for this new potential are listed in Table 6.1. We refer to the pseudopotential that is generated with nine valence electrons as hard since it will require more planewaves than a typical soft pseudopotential. By treating both the $4s$ and $4p$ states as valence states, the calculated total energy of the system will be shifted downward by the binding energy of these states in comparison to the total energy calculated with the soft potential. In the calculations shown in the preceding chapter, with the soft pseudopotential, this binding energy was treated as constant was therefore neglected.

Energy convergence tests show that an energy cutoff of 60 Ry is sufficient and a similar number of k -points was adequate as compared to the number required for the soft pseudopotential. We can estimate that we are within about 20 meV of the ground state based on calculations similar to those of Table 5.1 with an energy cutoff of 60 Ry. Convergence of the equation of state parameters can be seen in Table 6.1

Potential	Ecut (Ry)	k -points	E_0 (eV)	V_0 (a_0)	B_0 (GPa)	B'_0
soft	10	26	-17.244	519	3.57	3.52
soft	15	26	-17.184	516	3.64	3.71
hard	60	14	-678.275	526	3.60	3.50
hard	60	26	-678.250	526	3.52	3.52
hard	100	14	-678.281	526	3.60	3.62

Table 6.1: The fitted parameters to the Murnaghan equation of state for the hard pseudopotential as compared to those obtained with the soft pseudopotential.

where we look at the change in the fitted parameters with different values for the energy cutoffs and different numbers of k -points. By glancing at Table 6.1, the differences between the hard and soft pseudopotentials are almost constant, which one may consider to be the binding energy of the $4s$ and $4p$ states. To examine the issue closely, in Fig. 6.1 we plot both the hard and soft bcc energy-volume curves except the soft potential is manually shifted down in energy to make up for the binding energy difference.

Now the detailed differences can be seen. Near the equilibrium volume of ($V = 520 a_0^3/\text{atom}$), the curves are almost identical, but at small volumes, the curves deviate with the soft pseudopotential being lower in energy than the hard pseudopotential. This indicates that the hard pseudopotential is behaving correctly at small atomic volumes, where as the soft pseudopotential is not. One final check is to look for the fcc to bcc transition volume as we did with the soft potential. In Fig. 6.2, we plot the energy-volume curves for both the fcc and bcc structures with 60 Rydbergs as the energy cutoff and 26 k -points. Here the bcc structure is plotted

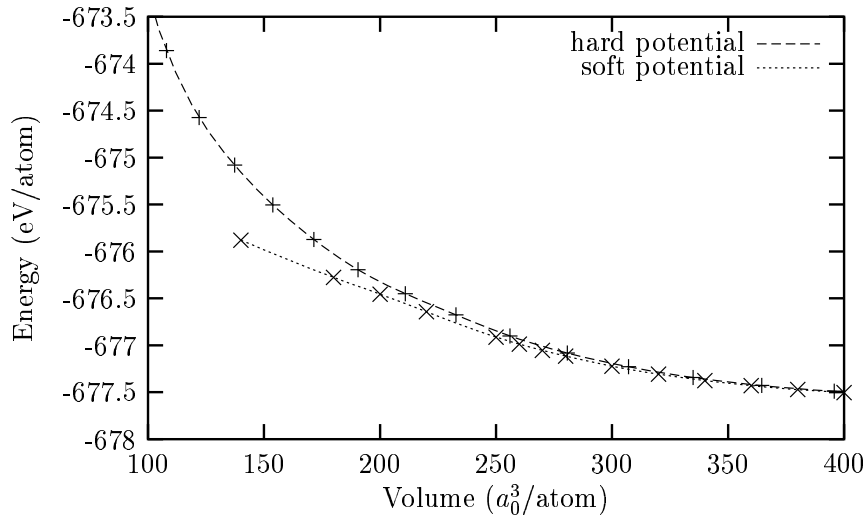


Figure 6.1: This energy-volume curves for the hard and soft pseudopotentials. The energy of soft pseudopotential is shifted down in energy by 661.032 eV to make up for the difference in binding energy between the two calculations. At small volumes the soft pseudopotential has lower energy than the hard pseudopotential which is were it fails.

using the fcc energy as the reference energy. The figure shows that the transition volume for the fcc to bcc transition is about $285a_0^3/\text{atom}$ which is closer to the experimental value of $300a_0^3/\text{atom}$ which was obtained by Schwarz *et. al.* [4]. We also plot the enthalpy of the two structures in Figure 6.3. From the enthalpy curve we find that the transition pressure is about 6 GPa which is a little smaller than the experimental value of 7 GPa. One may also notice that the bcc structure becomes slightly more favorable energetically than fcc in the 17 to 20 GPa range. What is interesting is that there is a turning point in the fcc structure around 13 GPa. This we believe to be an electronic structure change in the system. In Fig. 6.4 and Fig. 6.5, we show the band structures for the fcc structure near 0 GPa and 13 GPa,

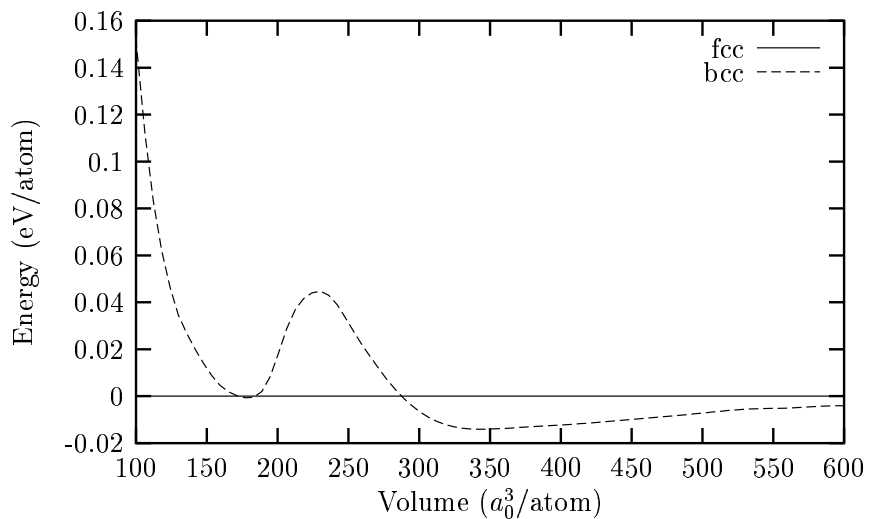


Figure 6.2: Energy-volume curves for the fcc and bcc structures. Here the fcc energy is used as the reference. The first crossing point for the two curves determines the transition volume of $285 a_0^3/\text{atom}$.

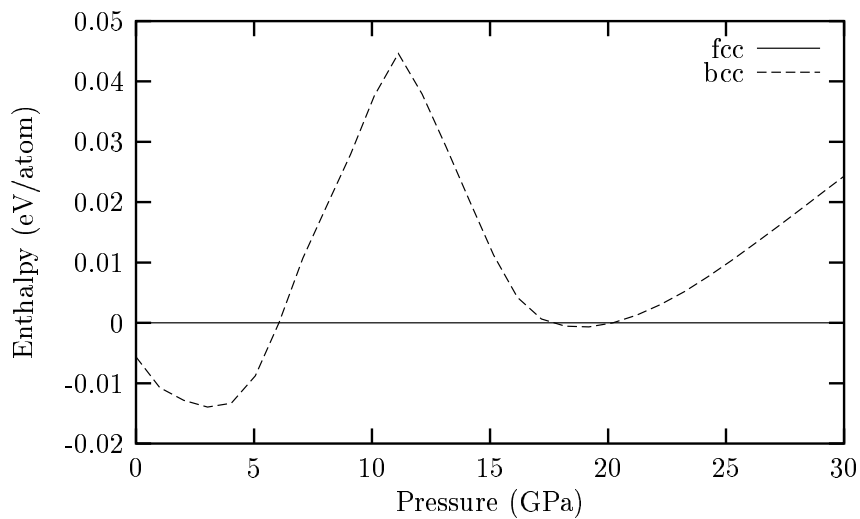


Figure 6.3: Enthalpy-pressure calculations for the fcc and bcc structures. Here the fcc enthalpy is used as the reference energy. The crossing point for the two curves determines the transition pressure of about 6 GPa.

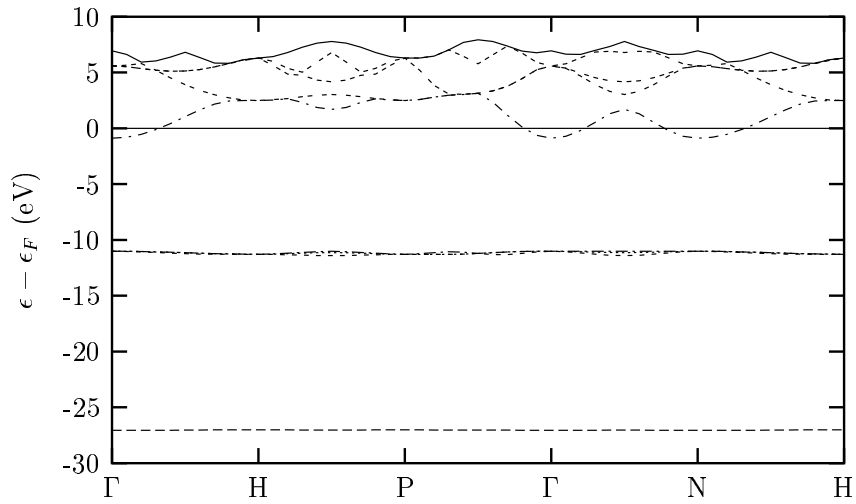


Figure 6.4: The band structure for bcc rubidium near zero pressure. The $4s$ and $4p$ bands appear quite narrow.

respectively. At 0 GPa, the core $4s$ and $4p$ bands are quite narrow, showing no overlap. At 13 GPa, one can see that more bands have dropped below the Fermi level. Because it is near this pressure where the $s \rightarrow d$ transition occurs, it can be assumed that this is the d orbital or at least some type of $s-d$ hybridized band crossing the Fermi level. These same characteristics are seen in similar band-structure calculations for cesium [45].

Another interesting point is that the $4s$ and $4p$ bands are also broaden significantly under pressure. In Fig. 6.6 we show the density of states for the fcc structure at 0 and 35 GPa. At low pressure, the $4s$ and $4p$ bands are quite narrow and under pressure the $4p$ broadens significantly. We now believe we have a working pseudopotential that gives reasonably accurate results for the low pressure bcc and fcc phases. Although the LDA is overbinding and gives slightly smaller equilibrium

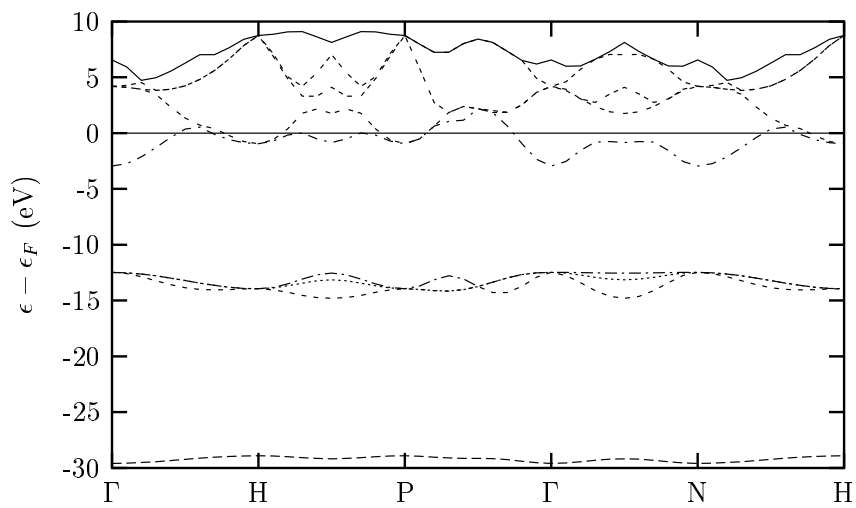


Figure 6.5: The band structure for bcc rubidium near 13 GPa. The core $4s$ and $4p$ bands have broadened and more states have dropped below the Fermi level.

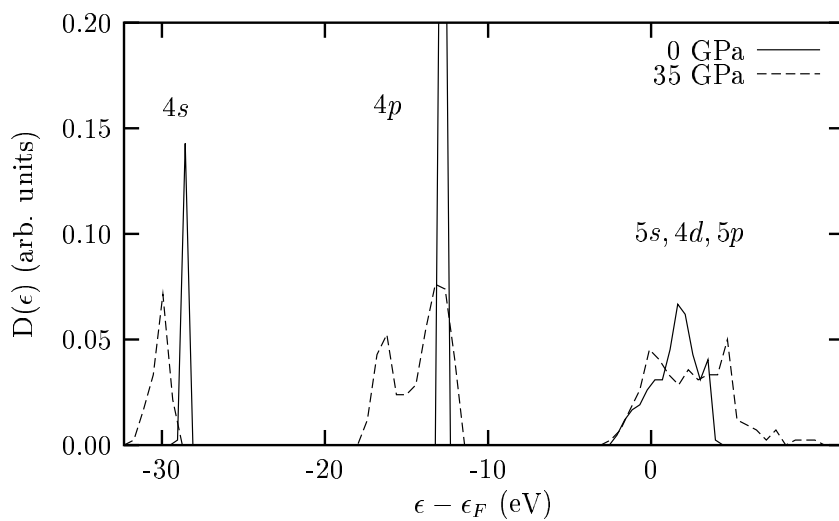


Figure 6.6: The density of states for the fcc structure at pressures of 0 and 35 GPa. Under pressure the semi core $4s$ and $4p$ show significant broadening.

volumes, the enthalpy appears to be correct giving the correct transition pressure. The deficiency in the pseudopotential in Chapter 5 was approximating that the $4s$ and $4p$ shells were inert under pressure which appear to be quite active under high pressure.

6.1 Complex Structures

Now that a working pseudopotential has been found, we can begin by calculating the stability of the currently known structures. In Fig. 6.7 we plot the energy against volume for all of the complex structures using fcc as the reference energy. For each structure, we used the lattice ratios and atomic coordinates obtained experimentally [2, 3, 4]. This leads to small errors on the order of our original error of about 20 meV. For the Rb V structure, 42 k -points were used while in the Rb VI structure only 5 k -points were used. Increased k -point sets showed to smooth the curves out slightly and did not change the energy beyond the error estimated earlier of about 20 meV. In Fig. 6.7, at small volumes the Rb VI structure is most stable. At about $V = 124a_0^3/\text{atom}$ there is a transition to Rb V. Experimentally, the Rb VI phase is identified at only one volume of $V = 120a_0^3/\text{atom}$. Throughout the entire regime of volume, the Rb IV structure is completely unstable. This calculation was done with full occupancy of the Wyckoff $4b$ sites and therefore treatment of this structure as a fully ordered one may be at fault.

We can also plot the pressure against the volume for each of the structures.

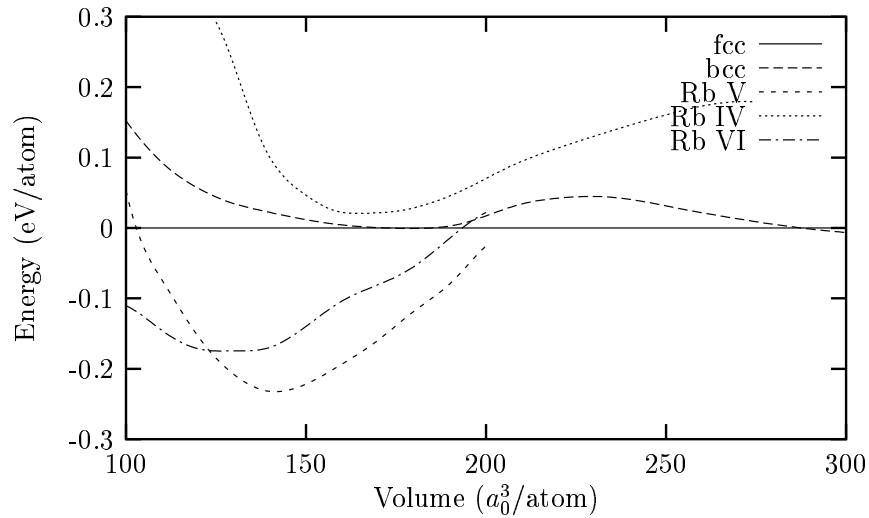


Figure 6.7: Total energy versus volume for the known structures of rubidium. The small wiggles in the curves are due to the use of cubic splines.

This is shown in Fig. 6.8 where we compare our results with the experimental data provided by Holzzapfel *et. al.* from reference [2]. At low pressures the LDA underestimates the atomic volume while at high pressures the disagreement is less. Small kinks in the pressure volume curves are due to electronic structure changes. For example, in the bcc pressure-volume curve, this occurs around 11 GPa. From the band structure calculation of Fig. 6.5, this is where a band drops below the Fermi surface. Similar effects are seen in the other structures at different pressures and volumes.

In Fig. 6.9, the enthalpy-pressure curves for all of the known structures for the five phases of rubidium are plotted. Each structure is plotted with respect to the fcc enthalpy. In Fig. 6.9, one can see that the Rb IV structure is not as stable as the fcc structure. The Rb V and Rb VI structures are quite stable with respect to the

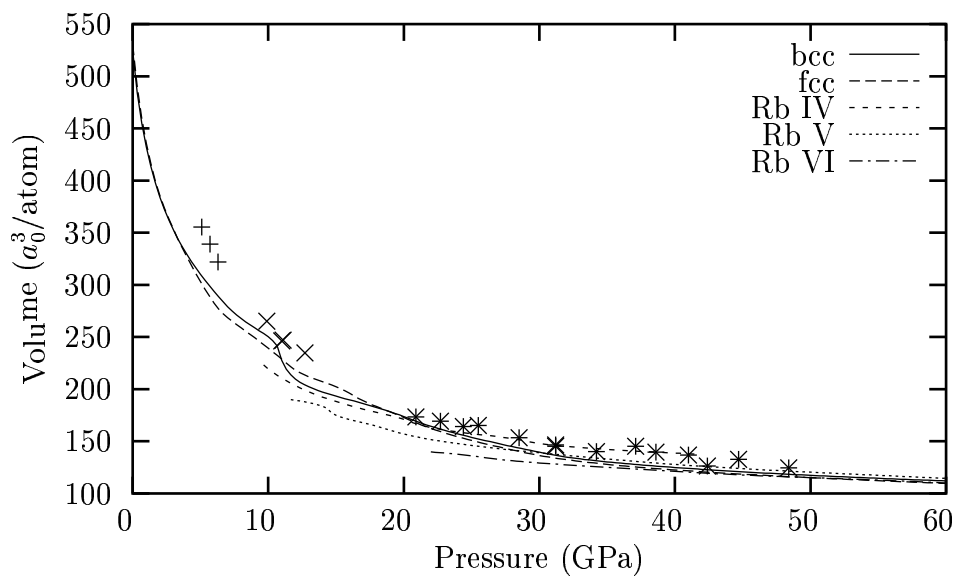


Figure 6.8: Pressure-volume curves for the five known phases of rubidium. The data points are the experimental pressure versus volume data from reference [2].

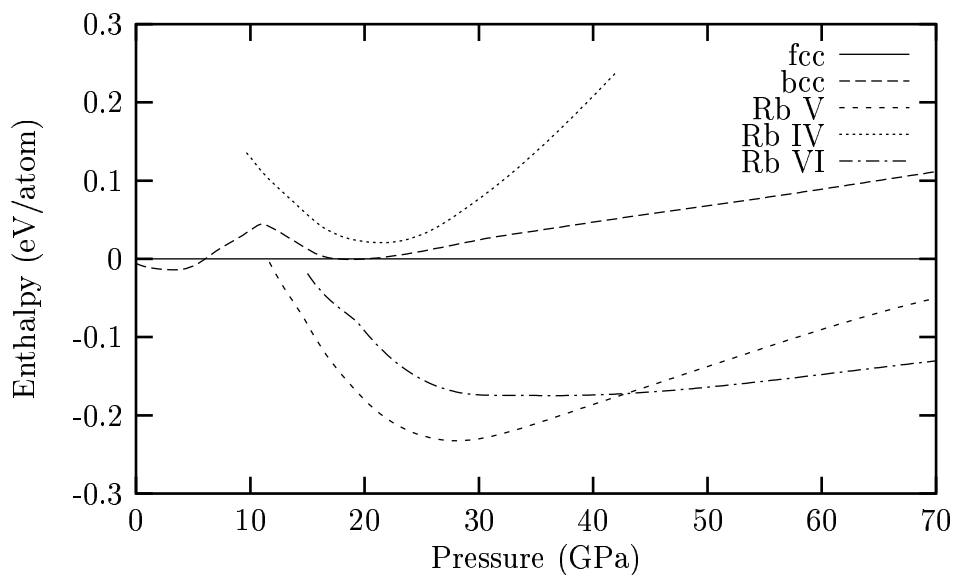


Figure 6.9: Enthalpy-pressure curves for the known structures of rubidium. Here the fcc enthalpy is used as the reference.

fcc structure and a transition pressure of 42 GPa is obtained for the Rb V to Rb VI transition. Experimentally the transition pressure is 46 GPa for this transition [2].

It would appear that we do have a working pseudopotential for rubidium throughout the entire pressure range, but we are still lacking in the proper treatment of the Rb IV structure.

6.2 Rubidium IV

In the previous section, the calculations showed that the Rb IV structure with full occupancy of the $4b$ sites was unstable with respect to the fcc structure and much higher in energy than the Rb V structure. Experimentally, this was only one possible solution for the structure. Another possible solution the experimentally obtained for the structure of Rb IV used $1/2$ occupancies of the $8g$ sites instead of full occupancy of the $4b$ sites [4]. This means that on average, 1 atom is sitting on two possible $8g$ sites (see Fig. 1.2). We tried various configurations for the $8g$ sites and found that it just raised the energy of the structure. When looking at the electron density of the fully occupied $4b$ structure along the z axis, it was observed that the system seemed compressed along the z direction. To relieve this stress, c/a was increased to see how the energy was affected. In Fig. 6.10, we plot the energy against c/a for the Rb IV structure, with full occupancy of the $4b$ sites, at $V = 170$ (a_0^3/atom) of the Rb IV structure. The value for c/a obtained experimentally is 0.500 which increases under pressure to 0.507 [4]. By increasing the value of c/a for the Rb IV

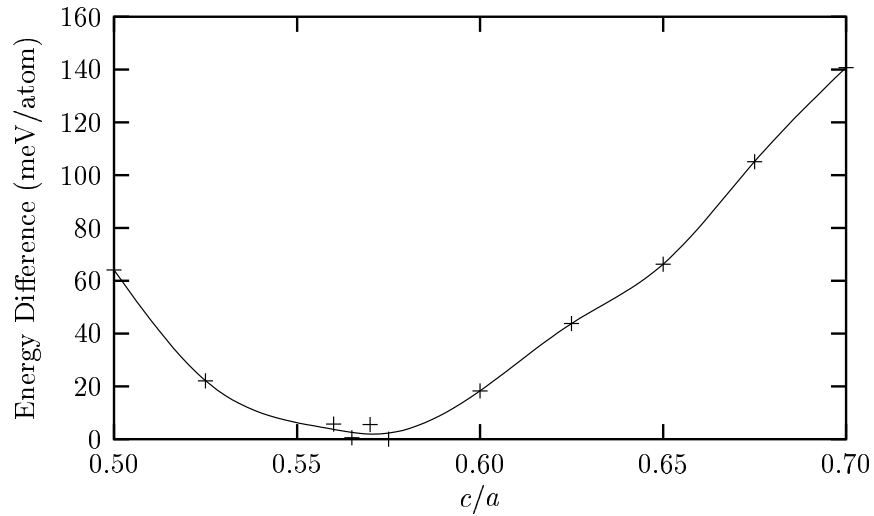


Figure 6.10: This is a plot of the relative lowering of the energy of the Rb IV structure with 1 atom in each of the $4b$ sites. The energy is lowered by about 60 meV when c/a is increased to approximately 0.57 from the experimental value of 0.50.

structure, one finds that when $c/a = 0.57$, one lowers the energy by about 60 meV.

The exact minimum cannot be resolved without relaxing the structure and also the fluctuations are within our error of about 20 meV. In Fig. 6.11, the enthalpy for the Rb IV structure with the increased value of $c/a = 0.57$ and full occupancy of the $4b$ is plotted with the previous calculations. From Fig. 6.11 one can see that the increased value for c/a does lower the energy of the structure, but not enough to stabilize it against Rb V. This tells us that the full occupancy of the $4b$ sites stretches the crystal along the z direction. At this point our only choice is to remove atoms from the unit cell. The removal of atoms from specific sites be a more drastic change in the structure than the variation of c/a . Therefore, we must allow the structure to relax to make up for the spaces left by the atoms removed. This takes us to a

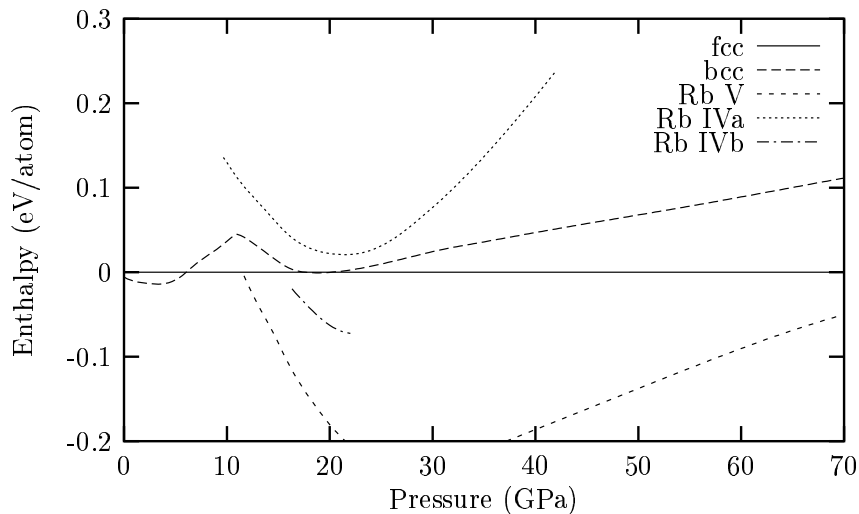


Figure 6.11: This plot is similar to Fig. 6.9 except now we add the enthalpy calculation for the Rb IV structure with $c/a = 0.570$, This is labeled as Rb IVb. The original calculation with $c/a = 0.500$ is labeled as IVa.

second technique which is quite powerful with the density functional method. The structures in the unit cell can be relaxed by calculating the forces on the atoms via the Hellman–Feynman theorem [46, 47]. This theorem gives the force on atom i as

$$\mathbf{F}_i = -\frac{\partial}{\partial \mathbf{R}_i} E[n(\mathbf{r})] \quad (6.1)$$

where \mathbf{R}_i is the position vector of the i_{th} nuclei and $E[n(\mathbf{r})]$ is the energy functional. Once the forces on the atoms have converged, the atoms are allowed to move under a damped Verlet molecular dynamics scheme [35]. The motion of the nuclei is allowed to evolve until adequate convergence to a stationary structure is achieved.

In Table 6.2 we all of the possible starting configurations for the initial positions of the atoms in the $4b$ sites. For the following calculations c/a will be fixed at the

Configuration	x	y	$z = 0.25$	$z = 0.75$
Rb ₁₆	0.5	0.0	o	o
	0.0	0.5	o	o
Rb ₁₇	0.5	0.0	x	o
	0.0	0.5	o	o
Rb _{18a}	0.5	0.0	x	o
	0.0	0.5	x	o
Rb _{18b}	0.5	0.0	x	o
	0.0	0.5	o	x
Rb _{18c}	0.5	0.0	x	x
	0.0	0.5	o	o
Rb ₁₉	0.5	0.0	x	x
	0.0	0.5	o	x

Table 6.2: In this table the starting coordinates of the atoms in the $4b$ sites for the Rb IV calculation are listed. The coordinates are listed in units of the appropriate lattice vector. The x's correspond to occupied sites while the o's are unoccupied.

experimental value of 0.5. If this were allowed to vary, we would have results that would completely disagree with the experimental observation. For each of these possible structures, calculations were carried out to find the ground state energy at $V = 170a_0^3/\text{atom}$ with 12 k -points in the Brillouin zone with out any symmetry constraints what so ever.

The structural relaxation was continued until the energy change per structural optimization step was approximatley 1 meV. These calculations were done on a Cray T3E with CPU time granted by the National Partnership for Advanced Computational Infrastructure. The computational requirements for each individual calculation took approximately 40 hours on 16 processors. The results of the minimized energy for all of the structures are given in Table 6.3. This table shows that 1/2

Structure Configuration	E_0 (eV/atom)
Rb ₁₆	-675.540
Rb _{18a}	-675.838
Rb _{18b}	-675.839
Rb _{18c}	-675.659
Rb ₁₉	-675.813
Fully occupied 4b	-675.824

Table 6.3: Here are the listed energies for the various possible configurations for atoms in the 4b sites listed in the Table 6.2.

occupation of the 4b sites is most energetically favorable in configurations Rb_{18a} and Rb_{18b}. Rb_{18c} is higher in energy due to the packing of the atoms in the 4b sites in the same channel along the z axis. This corresponds to 18 atoms per unit cell instead 20. Even though it does lower the energy, it is still as low as the Rb V energy of -676.0 eV/atom at $V = 170a_0^3/\text{atom}$. No drastic changes in the structure were observed in any of the relaxations. All atoms in the channels just sat in the 4b position. These values also tell us that the k -point sampling is not an issue since the energies did not change much with respect to the previous calculations. Now one is left with one more possibility, double the cell along the z axis to attempt to allow more disorder in the occupation of the sites.

If we increase the cell along the z axis, one has more options to work with, as far as the structure is concerned. If the 4b sites are not fully occupied, the structures may relax such that the atoms in other 4b sites move closer to one of the nearby 8g sites. By doubling the cell along the z direction, the length of the z axis to the same length as the x axis making the cell cubic. In Table 6.4 we list the configurations

Configuration	x	y	$z = 0.125$	$z = 0.375$	$z = 0.625$	$z = 0.875$
Rb_{38a}	0.5	0.0	x	x	o	x
	0.0	0.5	x	o	x	x
Rb_{38b}	0.5	0.0	x	x	o	x
	0.0	0.5	o	x	x	x
Rb_{38c}	0.5	0.0	x	x	o	x
	0.0	0.5	x	x	o	x

Table 6.4: In this table the starting coordinates of the atoms in the $4b$ for the unit cell doubled along the z axis. The coordinates are listed in units of the appropriate lattice vector. The x's correspond to occupied sites while the o's are unoccupied.

Structure Configuration	E_0 (eV/atom)
Rb_{38a}	-675.838
Rb_{38b}	-675.857
Rb_{38c}	-675.850
Fully occupied $4b$	-675.791

Table 6.5: Here are the listed energies for the various possible configurations for atoms in the $4b$ sites listed in Table 6.4.

we choose to calculate. Each calculation was carried out for 1 k -point and at an atomic volume of $V = 170 a_0^3/\text{atom}$.

In this case the configurations Rb_{38a} , Rb_{38b} , and Rb_{38c} all relaxed similarly. Two of the atoms relaxed to the $8g$ sites and one atom in between the two $8g$ sites stayed in the $4b$ site. It is at this time we should highlight the third result on the Rb IV structure which the experimental group identified [4]. It was not mentioned in the Chapter 1 because it was considered an over refinement by Schwarz *et. al.* A third solution for the structure was 0.17 occupancy of the $4b$, 0.35 occupancy of the $8g$ which corresponds to 19.48 atoms per unit cell. In our case, we have a 2 to 1 ratio

of occupancy of $4b$ to $8g$ sites and 38 atoms per unit cell which agrees quite nicely.

Enthalpy results for the Rb_{38c} structure showed results comparable with the results for the configuration of fully occupied $4b$ sites and $c/a = 0.570$. This is a step in the right direction since this calculation was done with $c/a = 1.0$ which corresponds to $c/a = 0.50$ with 18 atoms per cell. So it appears at this time that we have not found a valid unit cell representation for the Rb IV structure. Based on the structural relaxations, the atoms Wyckoff $16k$ sites do not move appreciably. We have also calculated that a full occupancy of the $4b$ sites is *not* energetically favorable. By varying the occupancy of various sites, we were able to lower the energy somewhat, but not enough to stabilize it against Rb V.

CHAPTER 7

CONCLUSIONS

It has been shown that density functional calculations can be a powerful tool. In the case of rubidium at high pressure, that this tool reproduces and confirms experimental results very well. We have confirmed the phase transitions for the bcc to fcc phase. As far as the Rb V to Rb VI transition, little is known experimentally [2, 3]. The Rb VI phase is known to exist at about 46 GPa, but the volume and pressure points for the specific transition are unknown. We have calculated the pressure for the transition to be 42 GPa and the transition volume to be $125 a_0^3/\text{atom}$.

Unfortunately, we were not able to find a correct unit cell description for the Rb IV structure. Many attempts we made and each attempt brought us closer to a possible unit cell description. If time had allowed, a study of all the possible occupancies of the enlarged cell might have given rise to a unit cell that could be a good enough model of the disordered Rb IV structure. These types of calculations are very difficult and require much computer time and resources.

Future calculations could be used to predict what structure the Rb III phase. Knowing that it might be close to the K III structure gives one enough information to get started. We have made some attempts at finding a stable structure, but none

that were energetically favorable have been found. Based on the relations between the phase diagrams between Rb and Cs one could predict the dhcp structure above the Rb VI phase. An estimate of that transition pressure would put it above 100 GPa which is quite high.

BIBLIOGRAPHY

- [1] M. Hanfland, K. Syassen, N. E. Christensen, and D. L. Novikov, *Nature (London)* **408**, 147 (2000).
- [2] M. Winzenick, V. Vijayakumar, and W. B. Holzapfel, *Phys. Rev. B* **50**, 12381 (1994).
- [3] U. Schwarz, K. Sysassen, A. Greztechnik, and M. Hanfland, *Solid State Comm.* **112** 319 (1999).
- [4] U. Schwarz, A. Greztechnik, K. Sysassen, I. Loa and M. Hanfland, *Phys. Rev. Lett.* **83** 4085 (1999).
- [5] K. Takemura, S. Minomura, and O. Shimomura, *Phys. Rev. Lett.* **49** 1817 (1982).
- [6] U. Schwarz, K. Takemura, M. Hanfland, and K. Syassen, *Phys. Rev. Lett.* **81** 2711 (1998).
- [7] K. Takemura, O. Shimomura and H. Fujihisa, *Phys. Rev. Lett.* **66** 2014 (1991).
- [8] W. B. Holzapfel and John Tse, *Private Communication*.
- [9] Waldemear Maysenholder, Steven G. Louie, and Marvin L. Cohen, *Phys. Rev. B* **31** 1817 (1985).
- [10] L. H. Yang, A. P. Smith, R. Benedek, and D. D. Koelling, *Phys. Rev. B* **47** 16101 (1993).
- [11] V. L. Sliwko, P. Mohn, K. Schwarz, and P. Blaha, *J. Phys: Condens. Matter* **8** 799 (1996).
- [12] H. L. Skriver *The LMTO Method* (Springer, Berlin, 1984).
- [13] A. K. McMahan, *Phys. Rev. B* **29**, 5982 (1984).
- [14] K. Takemura, N. E. Christensen, D. L. Novikov, K. Syassen, U. Schwarz, and M. Hanfland, *Phys. Rev. B* **61** 14399 (2000).

- [15] A. A. Katsnelson, V. S. Stepanyuk, A. I. Szasz, and O. V. Farberovich, *Computational Methods in Condensed Matter: Electronic Structure* (American Institute of Physics, New York, 1992).
- [16] J. C. Slater, Phys. Rev. **81**, 385 (1951).
- [17] J. C. Slater, *Quantum Theory of Matter* 2nd edition (McGraw-Hill, New York, 1964).
- [18] L. H. Thomas, Proc. Camb. Phil. Soc. , **23** 542 (1927).
- [19] E. Fermi, Z. Phys. **48** 73 (1928).
- [20] P. Hohenberg and W. Kohn, Phys. Rev. B **136**, 864 (1964).
- [21] W. Kohn and J. L. Sham, Phys. Rev. A **140**, 1133 (1965).
- [22] V. R. Shaginyan, Phys. Rev. A **47** 1507 (1993).
- [23] D. M. Ceperley and B. J. Alder, Phys. Rev. Lett. **45**, 567 (1980).
- [24] J. P. Perdew and A. Zunger, Phys. Rev. B **23**, 5048 (1981).
- [25] R. Car and M. Parinello, Phys. Rev. Lett. **55**, 2741 (1985).
- [26] M. C. Payne, M. P. Teter, D. C. Allan, T. A. Arias, and J. D. Joannopoulos, Rev. Mod. Phys. **64**, 1045 (1992).
- [27] L. Verlet, Phys. Rev. Lett. **159**, 89 (1967).
- [28] D. R. Hamann, Phys. Rev. B **40**, 2980 (1989).
- [29] N. Troullier and J. L. Martins, Phys. Rev. B **43**, 993 (1991).
- [30] L. Kleinman and D. M. Bylander, Phys. Rev. Lett. **48**, 1425 (1982).
- [31] X. Gonze, P. Kackell, and M. Scheffier, Phys. Rev. B **41**, 12264 (1990).
- [32] X. Gonze, P. Kackell, and M. Scheffier, Phys. Rev. B **44**, 8503 (1991).
- [33] D. Vanderbilt, Phys. Rev. B **41**, 7892 (1990).
- [34] S. G. Louie, S. Froyen, and M. L. Cohen, Phys. Rev. B **26**, 1738 (1982).
- [35] M. Bockstedte, A. Kley, and M. Scheffler, Comp. Phys. Comm. **107** 187 (1997).
- [36] C. Kittel, *Introduction to Solid State Physics*, (John Wiley and Sons, New York, 1976)

- [37] N. D. Mermin, Phys. Rev. A **137**, 1441 (1965).
- [38] D. L. Chadi and M. L. Cohen, Phys. Rev. B **8**, 5747 (1973).
- [39] H. J. Monkhorst and J. D. Pack, Phys. Rev. B **13**, 5188 (1976).
- [40] M. Fuchs, M. Scheffler, Comput. Phys. Commun. **119**, 67 (1999).
- [41] F. D. Murnaghan, Proc. Natl. Acad. Sci. USA **30**, 24 (1944)
- [42] M. S. Andersen and C. A. Swenson, Phys. Rev. B **28**, 5395 (1983).
- [43] 1991 *Landolt-Bornsten New Series* vol. 111/29a ed D. F. Nelson (heidleberg: Springer).
- [44] J. P. Perdew, K. Burke, and M. Erzerhof, Phys. Rev. Lett. **77**, 3865 (1996)
- [45] S. Calesi, A. Franchini, V. Bortolani, and S. Martinelli, Phys. Rev. B **59**, 11716 (1999)
- [46] H. Hellmann *Einführung in die Quantumchemie* (Leipzig, Franz Deutsche 1937).
- [47] P. R. Feynman, Phys. Rev. **56**, 340 (1939).

VITA

Graduate College
University of Nevada, Las Vegas

Anthony Jon Zukaitis

Local Address:

1418 Hometown Ave.
Henderson, Nevada 89014

Home Address:

105 2nd Ave. E.
Grand Marais, Minnesota 55604

Degrees:

Master of Science, Physics, 1998
University of Nevada, Las Vegas

Bachelor of Science, Physics, 1996
University of Wyoming, Laramie

Dissertation Title:

Density Functional Calculations of Rubidium under Pressure

Dissertation Examination Committee:

Chairperson, Dr. Tao Pang, Ph. D.
Committee Member, Dr. Changfeng Chen, Ph. D.
Committee Member, Dr. Stephen Lepp, Ph. D.
Graduate Faculty Representative, Dr. Kathleen Robins, Ph. D.